



# A new method to estimate the characteristic raindrop size from space-borne Doppler radars: Validation with the Monte Carlo model

Takahisa Kobayashi, Kazuhiko Masuda, Hiroshi Yamauchi, and Ahoro Adachi

Meteorological Research Institute, Tsukuba, Ibaraki, 305-0052, Japan

5 *Correspondence to:* Takahisa Kobayashi (kobayxx:ah.wakwak.com ,kobay@mri-jma.go.jp)

**Abstract.** A method to retrieve the mass-weighted mean raindrop diameter ( $D_m$ ) from a space-borne Doppler radar is presented for Ku, Ka and W-band radars. The contribution of the air motion to the measured Doppler velocities which are the sum of the raindrop fall velocity and the vertical velocity of the atmosphere ( $V_{air}$ ), was removed by a physically-based algorithm. The attenuation corrected reflectivity factors, the specific attenuation and the Doppler velocity are used as input in the algorithm to estimate  $D_m$  from the theoretical relationships among those values. For Ku-band, the effects of air motion were well removed, whereas the effects of DSD were difficult to remove due to the Rayleigh scattering regime. The latter effects were reduced by using a technique to determine an appropriate DSD by using the dependence of Z-R relationship on  $D_m$ . For W-band, modified algorithm were developed to estimate  $D_m$ . The validations of the retrieval method were made using simulated rain drop size distributions. A Monte Carlo model was used to evolves DSD by coalescence and breakup in a convective rain. Uncertainties in the retrieved  $D_m$  arising from the measurement errors were examined. The validation results show good agreement between the estimated  $D_m$  and the model values calculated from the simulated raindrop size distributions.

## 1 Introduction

Temporal and vertical variations of raindrop size distribution (DSD) are closely related to the process of precipitation system. Studies on the evolution of DSD is, therefore, crucial to improve our understating of the microphysics of rain. Ground-based measurements of DSD have been made with a disdrometer, and a wind profiler (e.g. Kobayashi and Adachi, 2001, 2005). Many simulation studies on the evolution of DSD have been also carried out (e.g. Khain et.al., 2000). These studies suggest that significant temporal and vertical variations appear in a convective rain. In addition to these variations, onset of rain, large raindrops are often observed at the ground because breakup process hardly occurs in lower altitudes. Whereas, frequent breakup events result in many small drops and intense rain as a chain reaction in mature stage of rain (Langmuir, 1948). The dual-polarized radar is a useful tool for measurements of DSD. Although it cannot derive the full shape of DSD, it can estimate the median volume diameter ( $D_0$ ) (Bringi et. al., 2006). The scatter plot of the relationships of measured  $D_0$  and rain rate shows that  $D_0$  tends to reaches an equilibrium value at high rain rate in a convective rain (Bringi et al., 2003). However, there are considerable variations of  $D_0$  for low rain rate and little correlations between  $D_0$  and rain rate.



30 These may be due to the variations of initial cloud properties and large rain drops evolved in the initial stage of rain as mentioned above. Another characteristic size, the mass-weighted mean diameter ( $D_m$ ) is the ratio of the fourth to third DSD moment and is also estimated from the dual-frequency radar equipped on the Global Precipitation Measurement (GPM) and is applied to study the precipitation system on a Global scale (Yamaji et al., 2021). The characteristic sizes are also expected to specify the life stages of rain.

35 The space-borne radar onboard the Precipitation Measuring Mission (PMM) satellite (Iki et al., 2025), which is currently being planned, will equip a single-frequency Doppler radar at Ku-band (KuDPR). The Earth Cloud Aerosol and Radiation Explorer (EarthCARE) satellite (Wehr et al., 2023) also equips a W-band cloud profiling Doppler radar (CPR). Since the radars onboard the PMM and EarthCARE are single-frequency Doppler radars, the method to derive  $D_m$  used in the Dual-frequency Precipitation radar (DPR) cannot be applied. Because the fall velocities of raindrops are related to their size, the  
40 mass-weighted mean diameter may be estimated from the Doppler velocity ( $V_p$ ) measured with the nadir pointing space-borne Doppler radars. However, the measured Doppler velocity is the sum of the raindrop fall velocity and the vertical velocity of the atmosphere ( $V_{air}$ ). Thus, the measured  $V_p$  cannot be directly applied to estimate  $D_m$  in the presence of air motion. To remove the effects of air motion from  $V_p$ , methods by using the differential Doppler velocity (DDV), which is a difference of  $V_p$  between two Doppler radars operated at different frequencies, has been studied (Williams et al., 2016,  
45 Matrosov, 2017, Mroz et al., 2020). This technique is useful but cannot be applied to the PMM and the EarthCARE. Estimation of  $V_{air}$  from the vertical profiles of the equivalent reflectivity factor ( $Z_e$ ) and  $V_p$  has been also developed for the EarthCARE (Sato et al., 2009, Kollias et al., 2023). Even if the effects of air motion are removed, it is necessary to assume DSD to derive  $D_m$  because the measured Doppler velocity observed is a reflectivity-weighted value.

In this paper, we propose a new method to estimate  $D_m$  from the measured values of  $V_p$ ,  $Z_e$ , and attenuation from the space-  
50 borne Doppler radar at Ku and W-band. Space-borne radars measure the path integrated attenuation (PIA) which is attenuation of cloud and precipitation from the surface to the satellite and is used for the attenuation correction. Thus, vertical profiles of rain attenuation can be estimated to some degree (Meneghini, and Nakamura, 1990, Iguchi, 2000, Seto et al., 2021, Kobayashi et al., 2022). In our method, the specific attenuation ( $k$ ) is used to determine the effects of air motion and DSD on  $V_p$ ; the method removes the effects of atmospheric vertical velocity from  $V_p$  and the effects of the DSD  
55 variations on the relationship between  $V_p$  and  $D_m$ , and estimates the correct  $D_m$ . Thus, the method is a physically-based algorithm and is different from the statistical approaches to derive  $D_m$  used in the EarthCARE product by Mroz et al. (2023).

To verify the method, we need realistic temporal and vertical variations of  $V_p$ ,  $D_m$ ,  $Z_e$  and the attenuation. Observation data are preferred for the validation, but are rare because the DSD varies significantly associated with the life cycle of precipitation, in particular for convective rain. Unfortunately, such data is very limited. We have, therefore decided to use a  
60 numerical model to evolve DSD and calculate  $V_p$ ,  $D_m$ ,  $Z_e$  and the specific attenuation from the DSD to simulate realistic temporal and vertical variations of DSD for validation instead. Extensive studies have been made on DSD evolution with the stochastic coalescence equation (SCE). However, SCE may not be suitable to simulate significant and realistic variations of DSD (Pruppacher and Klett, 1978, Bayewitz et al., 1974). In this paper, we intend to simulate realistic evolution of DSD to



65 validate the retrieval method in detail, therefore, we applied the Direct Monte Carlo method for the simulations which  
assumes less conditions and can evolve temporal and vertical variations of DSD for any rainfall intensity. The Monte Carlo  
model is a time-consuming process and is difficult to apply for models that incorporate both dynamical and microphysical  
processes. However, this is not serious in this study because we do not intend to link the DSD evolution model to such  
dynamic model but to just simulate the vertical variations of DSD evolved by coalescence and breakup processes.

70 In the next section, the modified Monte Carlo model is described. In section3, characteristics of the simulated temporal and  
vertical variations of DSD in convective rain will be shown. The detailed studies of DSD variations associated with the life  
cycle of rain are useful for error analysis of the retrieval method. In section4, a method to estimate  $D_m$  from the space-borne  
Doppler radar at Ku-band will be proposed and examined using the results of the Monte Carlo simulations. The method is  
also applied for W-band cloud profiling Doppler radar (CPR) which is currently used in the Earth Cloud Aerosol and  
Radiation Explorer (EarthCARE) satellite (Wehr et al., 2023). This CPR primarily targets clouds but can also measure weak  
75 rain. It is useful for understanding of the aerosol-cloud-rain interaction if the  $D_m$  of rain can be estimated from the CPR.  
There are some problems in applying the retrieval method to the W-band radar, such as significant attenuation, difficulties in  
determining the specific attenuation and correcting the Doppler folding error. In the retrieval from the CPR measurements,  
there are further more issues to be solved such as the multiple scattering, non-uniform beam filling, the satellite motion etc.  
These issues are beyond the work of the paper which propose a technique to derive  $D_m$ . In this paper, we do not address these  
80 issues but describe the theoretical base and the potential of the method.

## 2 A Monte Carlo model for temporal and vertical evolution of DSD (MonDrop)

The processes of precipitation formation are (1) nucleation, (2) condensation, (3) evaporation, and (4) coalescence and  
breakup. In this paper, we consider only the process (4) and make numerical simulations of the evolution of DSD. There are  
two models for this purpose: the continuous growth model and the stochastic growth model (Pruppacher and Klett, 1997).  
85 The former model is simple, but growth is generally slow and unrealistic (Houze, 1993). The latter is represented by an  
equation called the coagulation equation or stochastic coalescence equation (SCE) (Gillespie, 1975). Since the SCE cannot  
be solved for a realistic kernel analytically but can be solved only for a simple kernel, it is often solved numerically. Various  
methods have been developed (Berry and Reinhardt, 1974, Khain et.al., 2000). One of methods is the direct Monte Carlo  
approach which is more flexible. The Monte Carlo approaches by Gillespie (1975) is a method with less assumptions  
90 comparing with the other methods, and is used to validate other methods as a benchmark model.

Our approach is basically the same as the algorithm of Seeßelberg et al. (1996) which is a modified version of the method  
by Gillespie (1975) (appendix A) but we have further modified their method to calculate the temporal and vertical evolution  
of DSD, i.e., our model is a time dependent one-dimensional shaft model. The vertical profiles of cloud/rain drop size  
distributions and the air vertical velocity are given as initial values. The model allows time dependent vertical atmospheric  
95 velocity. The cloud and rain are given at any layers and at an arbitrary time, and the evolution of DSD by coalescence and



breakup is calculated during drops ascent and descent. Evaporation is not considered in this paper because it has no significant effect on the drop size distribution (List and McFarquhar, 1990).

This model allows detailed analysis of the mechanisms of the cloud and precipitation dynamics but here is used to calculate temporal and vertical evolutions of DSD from cloud evolved by coalescence and breakup for the validation of the method to estimate  $D_m$  from space-borne Doppler radars. The simulations aim to reproduce rain with falling velocity that is detectable by the Doppler radars. Therefore, DSD of small  $D_m$  like drizzle is not considered. More realistic variations of DSD, in particular for DSD at larger particles, are needed but are generally difficult. The proposed Monte Carlo model is suitable for the validation of the method to estimate  $D_m$ . We will briefly describe the modified algorithm.

A one-dimensional rain shaft Monte Carlo model was developed to calculate temporal and vertical evolutions of DSD (MonDrop) based on the algorithm of Gillespie, (1975) and Seeßelberg et al. (1996), which is a one-layer box model and does not consider vertical profiles (Appendix A). In the modified model, atmosphere is divided into layers in vertical. Raindrops moves from layer to layer associated with the air motion and the fall velocity. The cloud and rain are given at any layers and at an arbitrary time, and the evolution of DSD by coalescence and breakup is calculated. Cases of bounce are not taken into account. Spherical rain droplet and cloud particles are assumed. The algorithm of the model is as follows.

1. Define the initial time ( $T=0$ ), the end of the simulation ( $T_{max}$ ), and time step  $\Delta t$  during which the evolution of DSD by coalescence and breakup is simulated in all layers but raindrops remain in each layer. Define the highest altitude ( $Z_{max}$ ). The atmosphere is divided by  $\Delta Z$  in vertical. Set the minimum ( $r_{min}$ ) and maximum ( $r_{max}$ ) raindrop size. The raindrop size distribution is described by logarithmically spaced bins in radius. The initial volume  $V$ , initial DSD of cloud or/and rain, atmospheric conditions, the kernel and the coalescence efficiency are specified.
2. Calculate the time interval  $\tau$  that the collision occurs and specify colliding two raindrops by random numbers. Modify DSD by removing the colliding two drops and adding new created drops at all layers and recalculate the probability of collision.
3. Advance time by  $\tau$ . If time does not exceed step  $\Delta t$ , return to step 2.
4. Move drops associated with the fall velocity of drops and the air motion. Update the volume  $V$ , and the probability of collision.
5. It is possible to add cloud or/and rain and modify the atmospheric conditions.
6. Return to the step 2 until the time exceed  $T_{max}$ .

To consider statistical fluctuations, several runs (realizations) with the same initial values and different random numbers are carried out.

The probability of collision increases with the number concentration of drops. Therefore, the number of drops should be sufficiently large for accurate simulations. The number of particles in each bin is determined from the DSD in the simulation volume  $V$ . Larger volume, therefore is needed, but requires more CPU time. When beginning calculation of developing process from cloud to rain, large number concentrations of cloud drops exist. As the cloud drops grow, the number of drops decreases. The optimum volume, therefore is difficult to determine. In model, the volume is determined so that the collisions



130 occur in certain times ( $t_{ref}$ ). The collection kernel is  $10^{-6}$ - $10^{-7}$   $\text{cm}^3 \text{sec}^{-1}$  for a particle size of 10  $\mu\text{m}$  (Pruppacher and Keltt, 1997, Long, 1974), and the particle number concentration is about  $10^9$  ( $\text{m}^{-3}$ ) for liquid water content  $\text{LWC}=1\text{gm}^{-3}$ . When the particle size distribution is assumed to be the Martial-Palmer distribution (Marshall and Palmer,1948), the average collision rate is about  $10^{-4}$  sec at 10 dBZ and  $10^{-3}$  sec at 30 dBZ (Rogers, 1989). Considering above issues, the volume (initial  $V=1$   $\text{cm}^3$ ) increases by assuming  $t_{ref} = 10^{-2}$ - $10^{-3}$  sec. Note the volume increases with time significantly. This technique was  
135 justified by confirming similar results of a single run to their average of several runs (Seeßelberg et al., 1996).

To calculate the vertical profiles of DSD, atmosphere is divided into  $N_L$  layers with the vertical resolution  $\Delta z$ . The model simulates the evolution of DSD in each layer in  $\Delta t$ . Then, the drops ascend or descend associated with the fall velocity and the air motion. Some drops remain in the same layer and others move into other layers. In the model, a fraction of a drop distributed to any layers is calculated as follows. Consider a drop with a velocity  $V_i$  (falling velocity of drops-atmospheric  
140 velocity) in layer  $L_i$ . The length of the moving distance of a drop from the upper boundary of the layer  $L_{topi}$  is written as  $\Delta L_{topi} = L_{topi} - V_i \Delta t$  and from the lower boundary  $L_{boti}$  is  $\Delta L_{boti} = L_{boti} - V_i \Delta t$ . Take minimum values of  $\Delta L_{topi}$  and  $L_{topj}$  and maximum values of  $\Delta L_{boti}$  and  $L_{botj}$  for all layers ( $j=1, \dots, N_L$ ). The fraction of a drop in layer  $L_i$  that is distributed to layer  $L_j$  ( $j=1 \dots N_L$ ),  $R_p(i, j)$  is determined as

$$R_p(i, j) = \frac{\min(\Delta L_{topi}, L_{topj}) - \max(\Delta L_{boti}, L_{botj})}{L_{topi} - L_{boti}}, \quad (1)$$

145 where  $\min(a, b)$  and  $\max(a, b)$  denote minimum and maximum values of  $a$  and  $b$  respectively. For  $R_p(i, j) \leq 0$ , the fraction in layer  $j$  is 0. This process is performed for all particles and layers. Small vertical grid spacing allows detailed vertical variations of DSD, however larger number of grids needs more CPU time. Whereas large grid spacing results in erroneous results. A vertical resolution of  $\Delta z$  of 10 to 40 m may be appropriate associated with a maximum fall velocity of  $10 \text{ms}^{-1}$  (Barthes et al., 2013, Hu and Srivastava 1995). In the present calculation,  $\Delta z = 20\text{m}$  was applied.

150 In this paper, the collision efficiency which is the ratio of collision cross section to the geometric cross section, is set to be unity considering the fact that the raindrop size is larger than 0.1 mm. The coalescence efficiency was calculated by Low and List (1982a). The effect of turbulence is not considered. For breakup, the probabilities of the occurrence of the filament, sheet, and disk types were considered. The DSD of each type of breakup was determined by Low and List (1982b). The method was verified by comparing with the simulations by Seeßelberg et al. (1996) and Low and List (1982b). Note, the  
155 rate of breakup was assumed to be  $(1-E_{coal})$  and for  $D_L < 0.2\text{mm}$ ,  $E_{coal}=1$ .

### 3 Temporal and vertical variations of DSD

In this section, we will present the temporal and vertical variations of DSD in a convective rain by using the MonDrop model. Simple convective rain models were considered in which cloud drops in lower altitudes ascend within updrafts and grow to raindrops, then descend. When raindrops descend, they further grow by coalescence and breakup. In the developing  
160 stage of rain, the mean raindrop size generally tends to increase with rain rate ( $R$ ) and reaches the equilibrium size for intense



rain. In the dissipating stage, the opposite is true. The mean drop size, therefore expected to be positively correlated to rain rate. However, measured relationships between  $D_0$  and rain rate in a convective rain show less correlations. Considerable scatter appears between  $D_0$  and rain rate in particular for small drops (Bringi et al., 2003). This suggests significant variations of DSD in the life cycle of rain. The object of the simulations is not to make detailed analysis of rain formation  
 165 process but to reproduce such variations for the validation of the retrieval method. Although the Monte Carlo model does not account for the effects of turbulence and evaporation in the present calculations, frequent events of coalescence and breakup possibility result in the significant variations of DSD. Such variations are appropriate to validate the method to estimate  $D_m$  from the space-borne Doppler radars presented in the next section. In addition to this, studies on the variation of DSD and the relationships of  $D_m$  - rain rate, and  $D_m$  -  $Z_e$  are useful to improve our understanding of the microphysical properties of rain.  
 170 Here, we will focus on the variations of  $D_m$  -  $Z_e$  relationships in the life cycle of rain. Note  $Z_e$  for C-band is applied.

Cloud particles and raindrops were assumed to be spherical, and ice particles were not considered. The simulations were made from the ground to 5 km in altitude with the vertical resolution of  $\Delta Z=20\text{m}$ . Figure 1 shows a schematic figure of the convective rain model. Initial clouds at an altitude from 2 to 3.5 km ascend within updraft air. Clouds were also added at time 200 and 400 sec. The upward air velocity ( $W_0$ ) was given from the ground to 4.5 km in altitude from time=0 to 400sec  
 175 after which no updrafts were assumed. Constant air speed was assumed for all layers which may not be so realistic but results in similar DSD variations for decreasing air speed with altitude linearly which are used for validations shown in section 5. The size distribution of the initial cloud was assumed to be the three-parameter gamma function as

$$N(D) = N_0 D^\mu \exp(-\lambda D), \quad (2)$$

where  $N_0$ ,  $\mu$  (shape), and  $\lambda$  (slope parameter) are parameters that determine the number of particles and the characteristic size.  
 180 Here, the shape parameter  $\mu$  was fixed as 6 and the liquid water content was  $2 \text{ gm}^{-3}$  for DSD of initial cloud. The median volume diameters  $D_0$  were 0.1 and 0.2 mm. Drop diameters were divided into 400 logarithmically spaced bins from  $0.1 \mu\text{m}$  to 8 mm. The raindrop fall velocity was calculated using the formula by Atlas et al. (1973). Atmospheric conditions such as temperature, and density were given as the mid-latitude summer model tabulated by McClatchey et al., (1971) and were used to determine the fall velocities of drops and the refractive index used in the next section. A hydrodynamic kernel was used as  
 185 the collision kernel, and breakup was calculated according to Low and List (1982b) as described above. Numerical simulations were made with the time step of  $\Delta t=1 \text{ sec}$  and  $t_{ref}=5E-3 \text{ sec}$ . The characteristic size  $D_m$ , rain rate and  $Z_e$  were calculated from the simulated DSD.

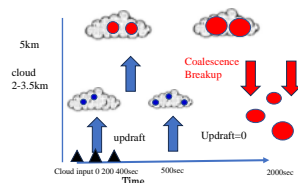


**Figure 1 Schematic figure of the simulated convective rain.**



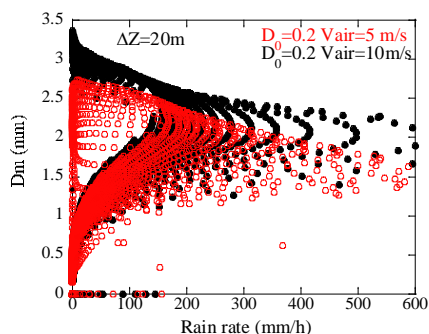
190 Figure 2 shows a scatter plot of  $D_m$  and rain rate calculated for all altitudes, time from 0 to 2000 sec and for various initial clouds of  $D_0$  and  $W_0$ . Red circles are for  $W_0=5 \text{ ms}^{-1}$ ,  $D_0$  of initial cloud as 0.2 mm, black dots are ( $D_0=0.2 \text{ mm}$ ) for  $W_0=10 \text{ ms}^{-1}$ . As rainfall rate increases,  $D_m$  tends to be constant about 2-2.5 mm for  $W_0=10 \text{ ms}^{-1}$ , which is considered to be an equilibrium state (Guangheng et al., 2019). Note the equilibrium DSD is independent of the initial characteristics of cloud. The equilibrium state cannot be reached for  $W_0=5 \text{ ms}^{-1}$ . For  $D_m$  smaller than the equilibrium size, the envelope of data ( $D_m$ ) is

195 positively correlated with rainfall rate, whereas negatively correlated for  $D_m$  larger than the equilibrium size. This relationship is similar to the relationship between  $D_0$  of rain and rainfall rate for one convective rain measured with the polarimetric radar S-band and a disdrometer (Bringi et al., 2003), which suggests that the Monte Carlo model succeeded in producing similar variations of DSD to the actual rain. Data in the positive correlations, i.e., area of  $D_m$  smaller than the equilibrium size may be in developing stage or dissipating stage. Whereas data in the negative correlations, i.e., area of  $D_m$

200 larger than the equilibrium size may indicate few large raindrops in the onset of rain. Large raindrops in upper layer fall rapidly due to sedimentation without suffering breakup.

Figure.3 shows time-height cross section of  $Z_e$  (a) and  $D_m$  (b). A precipitation core (here assumed to be an area of  $Z_e$  larger than 30dBZ) descends from 3.5 km to the ground. The peaks of  $Z_e$  appear at time of a little later than the time that the core was firstly observed at each altitude. Tendency of  $D_m$  is similar to  $Z_e$  but the peaks appear at the beginning of core i.e.,

205 before  $Z_e$  reaches its maximum. This suggests that larger and fewer raindrops descend more rapidly than smaller raindrops without breakup which results in large  $D_m$  and small  $Z_e$  at the beginning of rain. Similar tendencies have been reported from



210 **Figure 2 Scatter plot of rain rate and the mass-weighted mean diameter simulated for convective rain. Data for various initial conditions and vertical air motions are plotted.**



the ground-based radar measurements. The time-height cross section of  $Z_e$  and the differential reflectivity  $Z_{dr}$  in the precipitation core of convective rain observed by the dual-polarimetric radar shows that the time of the peak of  $Z_{dr}$  appears earlier than the peak of  $Z_e$  (Shusse et al., 2015). The differential reflectivity is a measure of the characteristic size of DSD (Bringi et. al, 2009), and therefore the tendency is consistent with the present calculations. The simulated results are well representative of the characteristics of the actual rain.

Figure 4 shows the vertical variation of DSD in the early stage of region (a) shows that higher concentrations of larger raindrops appear in lower altitudes. The temporal variations of DSD at altitude of 1 km (b) shows large drops appear in the early stage of rain and smaller raindrops increase with time at altitude of 1 km.

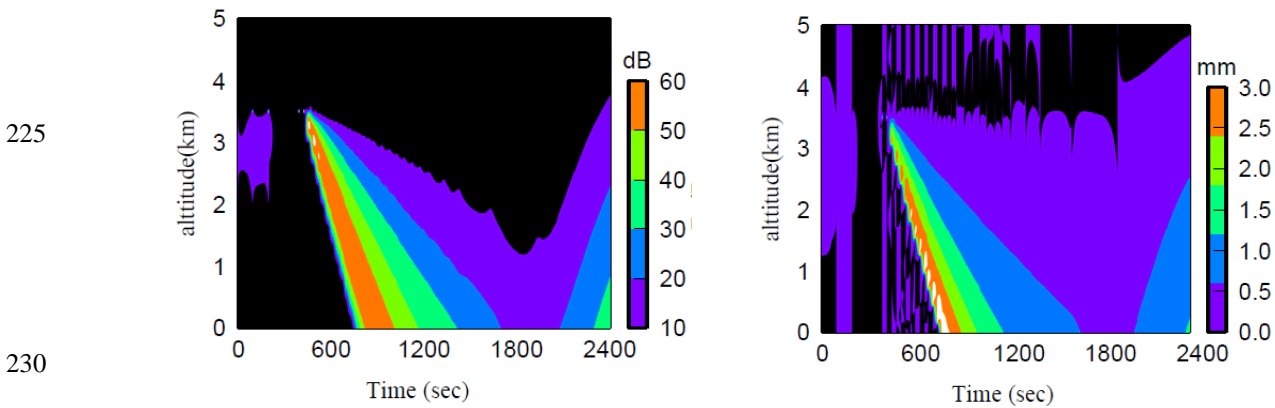


Fig. 3 Time-height cross sections of simulated  $Z_e$  (a) and  $D_m$  (b) for convective rain.

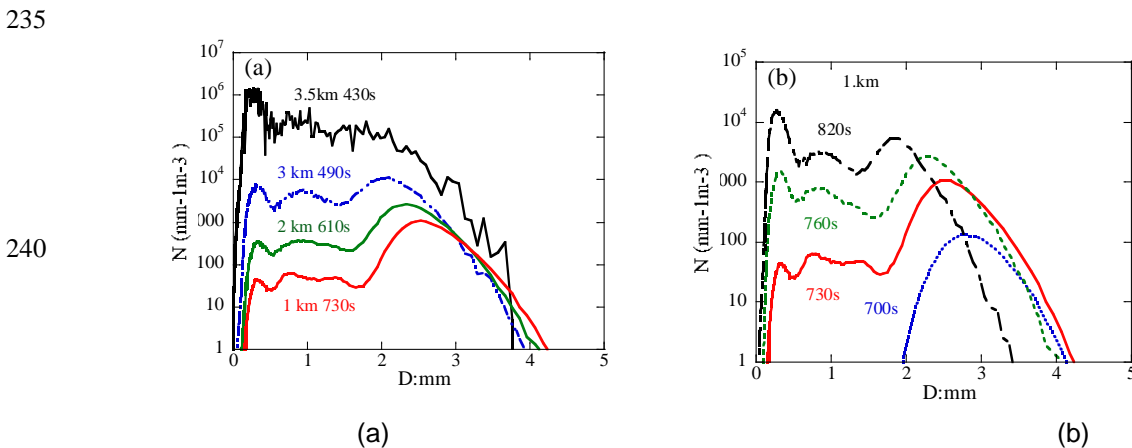


Fig. 4 Vertical variation of DSD in the core region (a) and temporal variation of DSD at altitude of 1 km (b).



Figure 5 shows the temporal variations of  $Z_e$ , and  $D_m$  at an altitude of 0.5 km. This figure clearly shows the difference in  
245 the time that the peak of  $Z_e$  and  $D_m$  appear as shown in Fig. 3. The largest  $D_m$  appears at time 720 sec whereas the maximum  
 $Z_e$  appears at 810 sec. Before 810 sec,  $D_m$  begins decreasing but  $Z_e$  still increases (negative correlation between  $D_m$  and  $Z_e$ )  
and after 810 sec both  $D_m$  and  $Z_e$  decrease (positive correlation). Opposite correlations appear between  $Z_e$  and  $D_m$ . The  
simulated DSDs show many larger raindrops and few small drops in lower altitudes at the beginning of rain whereas the  
different shape of DSD appears later. Figure 6a shows the scatter plots of  $D_m$  versus  $Z_e$  at the time before the core center (time  
250 of the maximum  $Z_e$ ) (red circles), at the core center (black squares) and after the core center (blue triangles) for a vertical  
velocity of  $W_0 = 10 \text{ ms}^{-1}$  and an initial cloud of  $D_0 = 0.2 \text{ mm}$ . The correlation between  $Z_e$  and  $D_m$  is positive for  $D_m < 2.5 \text{ mm}$ ,  
but negative for  $D_m > 2.5 \text{ mm}$  as shown in Fig.5. At  $D_m = 2.5$ , values of  $Z_e$  converge to high values of about 55 dBZ  
suggesting the equilibrium state. A similar tendency is obtained in the relationship between  $Z_e$  and rainfall rate. For weak  
updraft of  $W_0 = 5 \text{ m/s}$ , no clear positive or negative correlation is obtained. This is due to the insufficient development of  
255 raindrops in the upper altitudes.

Figure.6b shows the vertical profiles of  $Z_e$  and  $D_m$  at time before and after core center. At time before core center,  $D_m$   
increases toward the ground whereas  $Z_e$  tends to decrease indicating large raindrops evolved in upper layer fall due to  
sedimentation without collision. Decrease tendency in  $Z_e$  indicates fewer drop concentration in the lower altitude. Hereafter  
the raindrop size distribution in this period, referred as ‘DSDonset’. After the time of core center both  $D_m$  and  $Z_e$  increase  
260 toward the ground due to coalescence and breakup. Since the relationships of  $D_m - Z_e$  and  $Z_e - R$  change associated with the  
variations of DSD in life cycle of rain, the relationships can be used to identify the precipitation stage. This is important for  
accurate rainfall rate estimate, in particular for initiate of rain when estimating rainfall intensity from  $Z_e$ . The GPM-core  
satellite, equipped with dual-frequency radars, measures vertical profiles of  $Z_e$  and  $D_m$ . As mentioned, vertical variations of  
 $D_m$  are negatively related to  $Z_e$  at the beginning of rain in convective rain and  $D_m$  is positively correlated to  $Z_e$  in mature and  
265 dissipating stages. The behavior of the different correlations between  $Z_e$  and  $D_m$  in altitude, may be used to determine the life  
stage of rain from the GPM observations. In addition, realistic temporal and vertical variations of simulated DSD in a  
convective rain throughout the life cycle are useful to examine a method to estimate  $D_m$  from space-borne Doppler radars.

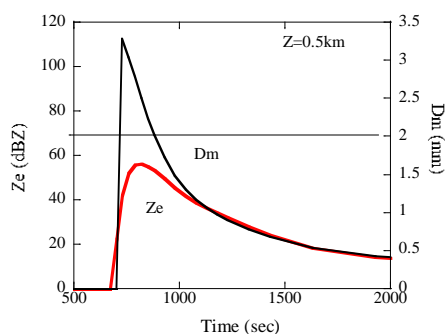


Fig. 5 Temporal variations of  $Z_e$ , and  $D_m$  at altitude of 0.5 km.



270

275

280

285

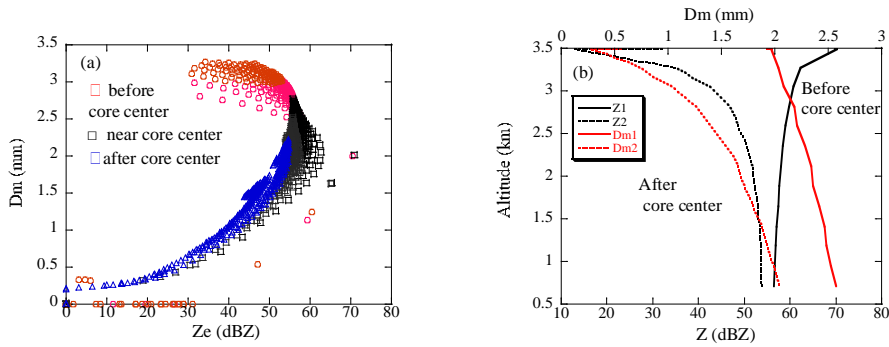


**Fig. 6** Scatter plots of  $D_m$  versus  $Z_e$ . Data at the core center (black), before (red), and after (blue) the time of core center are plotted (a). Vertical profiles of  $Z_e$  and  $D_m$  before ( $Z_1, D_{m1}$ ) and after ( $Z_2, D_{m2}$ ) the time of core center (b)

#### 4 A method to estimate $D_m$ from space-borne Doppler radars at Ku-band

The values of  $D_m$  are currently derived from the differential frequency ratio (DFR) measured with the Dual-frequency radar onboard the GPM core satellite. In the PMM, a single-frequency Doppler radar operated at Ku-band is currently planned. The EarthCARE satellite also equips a cloud profiling Doppler radar which operates at a single frequency of W-band. For these radars, the characteristic size of raindrops may be expected to estimate from the measured Doppler velocities instead of the DFR technique. The fall velocity of rain drops depends on the size, therefore  $D_m$  can be basically derived from the Doppler radars. There are, however, some problems to be solved in the retrieval of  $D_m$ . Here, we describe a method to estimate  $D_m$  from the space-borne Doppler radars.

The measured mean Doppler velocity ( $V_p$ ) depends on DSD, the wavelength of radar ( $\lambda$ ) and the air motion, and is given by

$$V_p(\lambda) = \frac{\int_0^\infty \sigma_b(D)N(D)V_f(D)dD}{\int_0^\infty \sigma_b(D)N(D)dD} + V_{air}, \quad (3)$$

where  $\sigma_b$  is the backscattering cross section,  $V_f$  is the fall velocity of raindrops and  $V_{air}$ , is the atmospheric vertical velocity. Given DSD,  $V_p$  and  $D_m$  correspond one-to-one. In addition, the measured Doppler velocity is affected by the air motion. Thus, in the estimate  $D_m$  from  $V_p$ , following issues should be considered:

- (1) The observed Doppler velocity is the sum of the reflectivity-weighted fall velocity of raindrops ( $V_D$ ) and the atmospheric vertical velocity  $V_{air}$ , it is, therefore necessary to remove  $V_{air}$  from  $V_p$ .



(2) Since the measured Doppler velocity is a reflectivity-weighted value, some information on the DSD or assuming DSD are needed.

305 The effect of (1) is more significant than (2) because the dependence of  $D_m$  on  $V_p$  is generally larger than the dependence of the DSD. In a convective rain, a strong updraft air motion will be found in the initial stage of rain and downdraft air motion will be found when raindrops are falling. The turbulence also leads to up or down draft. Even small atmospheric velocities (e.g., 0.25 ms<sup>-1</sup>) can cause large errors in the  $D_m$  estimated from  $V_p$  in particular for large size of raindrops (Mroz et al., 2020). To remove the effects of air motion, methods have been developed by using ground-based multi-frequency Doppler radars (Williams et al., 2016, Moroz et al., 2019, Matrosov, 2017). Another approach is to use statistical relationship  
310 between the amplitude of  $Z_e$  and  $V_D$  (eg., Kollias et al., 2023). A method to estimate  $V_{air}$  from the vertical profiles of  $Z_e$  and  $V_p$  has been also developed for the EarthCARE (Sato et al., 2009). Statistically, increases in the amplitude of  $Z_e$  are associated with  $V_D$ , i.e.  $D_m$  (e.g., Chen, 2022). For stratiform rain or cloud of small variability in the DSD, the effect of (2) may be less significant. However, as mentioned in the previous section, significant variations of the DSD are found in the convective rain, therefore the effect of (2) cannot be ignored.

315 To address these issues, another approach was applied in method. Because three parameters of  $V_{air}$  and the DSD (concentration and shape of the DSD) are unknown, another parameter except for  $Z_e$ ,  $V_p$  is needed to estimate  $D_m$ . Space-borne radars measure the path-integrated attenuation (PIA) which is the attenuation of radio wave from the surface to the satellite in the presence of precipitation. In the rainfall algorithm of the space-borne radar, the measured PIA is converted to the specific attenuation ( $k$ ) at each altitude (Meneghini, and Nakamura, 1990, Seto et al., 2021) and is used for the  
320 attenuation correction. In the method, the specific attenuation is used to specify and remove  $V_{air}$  and to consider the effects of the DSD. The combined effects of  $V_{air}$  and the DSD on the retrieval of  $D_m$  can be directly determined. The detailed algorithm will be shown later. Note that the attenuation-corrected reflectivity factors and the specific attenuation are assumed to be given.

For the Rayleigh regime, the specific attenuation does not depend on the shape of DSD significantly but is almost  
325 determined by the LWC, whereas,  $k$  depends on the DSD as well as LWC for the Mie regime. These features are shown in the relationships between  $k$  and  $D_m$  (Fig. 7) for the gamma size distribution of  $\mu=1, 3, \text{ and } 6$  at W and Ku-band, suggesting that  $k$  can be used to specify the effects of DSD in the retrieval of  $D_m$  from  $V_p$  for W-band. For Ku-band,  $k$  is not so sensitive to the DSD and is not so effective to identify DSD but is useful to determine the effects of  $V_{air}$  as well as for W-band. Because significant variations of the DSD at large raindrops appear in a real rain,  $k$  is useful to identify DSD to some degree  
330 even for Ku-band. The values of  $k$  are related to  $Z_e$  and  $D_m$  and can be used to specify the effects of  $V_{air}$  on the retrieval.

For the Mie regime, the sensitivity of  $k$  to the DSD leads to difficulties in the estimation. The amplitude of  $k$  increases monotonically with  $D_m$  in the Ku-band, whereas the amplitude of  $k$  increases with  $D_m$ , reaching a maximum at approximately  $D_m=1$  mm, and then decreases in the W-band. It is, therefore, difficult to determine the exact values of  $D_m$  from  $k$ . Furthermore, the Ku-band radar on the GPM can measure rain of a high reflectivity as 50dBZ, whereas the W-band radar can  
335 only measure light rain of  $Z_e$  about 20 dBZ and near top of rain layer for intense rain due to the significant attenuation and



the Mie scattering at the W-band. The KuDPR (Ku-band) is a radar to measure precipitation, whereas the CPR operated at W-band is a radar to primarily measure cloud. Considering these differences, the method to estimate  $D_m$  for Ku-band radar will be firstly described. Next, the modified method for W and Ka-band will be presented to examine the potential of the CPR in the measurements of rain. In estimating  $D_m$ , attenuation-corrected reflectivity factors are assumed. The validation of the method will be made by using the realistic DSD variation simulated in convective rain as mentioned in the previous section.

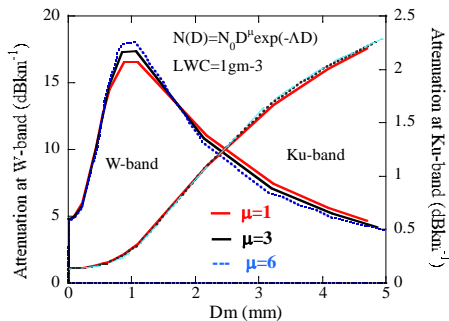


**Fig. 7 Specific attenuation vs  $D_m$  for the DSDs of the Gamma function. Various values of the shape parameter  $\mu$  ( $=1, 3, 6$ ) are plotted for W and Ku-band**

345

#### 4.1 A method for Ku-band radar

To assess the sensitivity of  $D_m$  to the Doppler velocity and  $k$ , we performed calculations for various DSDs by Mie theory. Figure 8 shows the representative calculations of the relationships between the measured reflectivity factor (attenuation corrected values  $Z_e$ ) and the Doppler velocity  $V_D$  ( $=V_p$  in the absence of atmospheric motion) for various values of  $D_m$  and  $k$  at Ku-band. Data calculated for DSD of the three parameter Gamma function of  $\mu = 3$  (Eq.2) are plotted. The horizontal lines represent  $Z_e$  and  $V_d$  that result for specified values of  $k$  and the vertical lines represent the values for specified values of  $D_m$ . The circle symbols shown in the figure represent the simulated values of  $Z_e$  and  $V_p$  in the convective rain (for  $LWC < 0.1 \text{ gm}^{-3}$ ) as mentioned in the previous section. The DSD's of strong initial upward velocity of  $10\text{ms}^{-1}$  were applied. This figure clearly illustrates a method for the simultaneous determination of  $D_m$  and  $k$  from the measured values of  $Z_e$  and  $V_p$ . However, as mentioned earlier, in the presence of air motion, the estimated values of  $D_m$  and  $k$  will be incorrect. Our object is to estimate  $D_m$ , therefore, the value of  $k$  obtained from the PIA is used as a parameter to constrain the effects instead of a parameter to be estimated. First, determine  $D_m$  and  $k$  from the measured  $Z_e$  and  $V_p$ . In the presence of air motion, incorrect

355

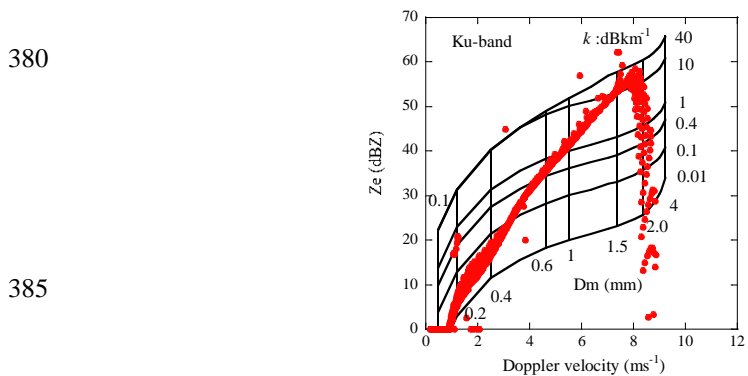


values of  $D_m$  and  $k$  are obtained. Then, change  $V_p$  and determine  $D_m$  and  $k$  again. Repeat this process until the estimated  $k$  matches the observed value and determine the correct value of  $D_m$ .

360 The Gamma function is often assumed for the DSD in the radar observations and the values of  $\mu = 3$  is used in the rain-rate estimate algorithm (Set et al., 2021, Adachi et al., 2015). However, such DSD is not true in a real rain as shown in Fig.4, In addition, the relationship between  $D_m$  and  $V_p$  depends on the parameter  $\mu$  as well (Battaglia et al., 2020). The actual raindrop size distribution is not accurately represented by the gamma function. Accurate estimation results can be expected by selecting a parameter  $\mu$  in the gamma function whose  $V_p - D_m$  relationship is similar to the observed one. In this section, the  
365 LUT assuming the values of  $\mu = 3$  is used to retrieve  $D_m$ . The fixed value results in bias errors depending on the DSD in measurements for Ku-band. The LUT with more appropriate  $\mu$  may be needed which will be discussed in section 4.3. The algorithm of the retrieval is as follows:

1. Estimate  $D_m$  from the measured  $V_p$  using the look up table (LUT: Fig.8) (Est1).
2. Estimate  $k$  from the measured  $V_p$  and the attenuated corrected  $Z_e$  using Figs. 8.
- 370 3. If estimated  $k$  differs from the measured value, estimate  $D_m$  and  $k$  again by changing  $V_p$  as  $V_p \pm \Delta V_p$ . The value of  $\Delta V_p$  was initially set, e.g., to be  $0.01 \text{ ms}^{-1}$ .
4. Estimate  $k$  for various values of  $\Delta V_p$  and select  $\Delta V_p$  that gives the minimum difference between estimated  $k$  and the measured  $k$ .
5. The optimum  $D_m$  is determined (Est2).

375 These procedures correct both effects of the air motion on  $V_p$  and the difference between the actual DSD and that applied in Fig. 8. If the actual DSD is close to the DSD applied in Fig. 8 and in the absence of air motion, selected  $V_p$  coincides with  $V_D$ , i.e., uncorrected  $D_m$  (Est1) coincides with the corrected value (Est2).



390 **Fig. 8 Theoretical relationships between  $Z_e$  and the Doppler velocities for various values of  $D_m$  and  $k$  for the Gamma DSD at Ku-band. Simulated data in a convective rain are also plotted (red circles).**



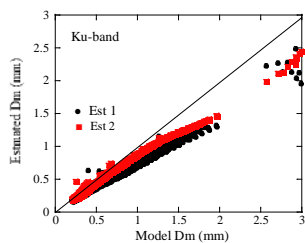
Validation of the retrieval was made using the DSDs at various altitudes and times evolved by the Monte Carlo model. The Doppler velocities, reflectivity factors, specific attenuations and  $D_m$ s were calculated from the DSDs and were used for the validation. In Fig. 9, the retrieved  $D_m$  values are plotted against calculated (model) values of  $D_m$  from the DSDs for  $W_0=10 \text{ ms}^{-1}$ . The vertical velocities of the atmosphere are zero for most data. The black circles represent the uncorrected values of  $D_m$  ( $D_m^{Est1}$ ), i.e., estimated from the calculated (observed)  $V_p$ . The red square symbols represent values of  $D_m$  ( $D_m^{Est2}$ ) estimated from  $Z_e$ ,  $k$  and the modified  $V_p$  using the LUT. Data of  $Z_e < 50 \text{ dBZ}$  are plotted. The uncorrected values  $D_m^{Est1}$  are underestimated in particular for large values of  $D_m$ . Whereas,  $D_m^{Est2}$  are closer to the model values. These data are thought to be in still air, so that the reason of the discrepancies is the differences of the measured (simulated) DSD from the DSD applied in the LUT. One of measures to identify DSD is a relationship between the Doppler velocities and  $D_m$  which depends on the shape of DSD. Figure 10 shows relationships of  $V_p$  and  $D_m$  (black square:  $W_0=3 \text{ ms}^{-1}$ , red:  $10 \text{ ms}^{-1}$ ) calculated from the simulated DSDs. The relationships for various Gamma DSDs of  $\mu =1$  (blue line), 3 (red) and 12 (green) are also plotted. The simulated values of  $V_p$  are smaller than the those of the Gamma DSD. When the relationships of the simulated data of  $V_p$  and  $D_m$  are fitted by the Gamma function, the fitted values of  $\mu$  may be larger than 3. For DSD of the Gamma function,  $V_D$  tends to increase with decreases in the parameter  $\mu$  at specified values of  $D_m$  for the Rayleigh regime (William et al., 2016, Mroz et al., 2020). This indicates that the uncorrected  $D_m^{Est1}$  will be underestimated if the fitted parameter  $\mu$  of the DSD in the measurement is larger than that of the LUT and vice-versa. The errors in the corrected values of  $D_m^{Est2}$  are significantly reduced but are still underestimated. This is because the correction using the attenuation is not so effective to identify DSD for the Rayleigh scattering as mentioned earlier. Figure 11 is the same as Fig.9 but for simulated DSD for initial upward air velocity  $W_0=3 \text{ ms}^{-1}$ . In this case, relationship of  $V_p$  and  $D_m$  is closer to that of the LUT ( $\mu=3$ ) for small values of  $D_m$  but larger for  $D_m > 0.5 \text{ mm}$ . The corrected values  $D_m^{Est2}$ , are therefore less underestimated and overestimated at  $D_m =0.5\text{mm}$ . Errors increase with  $D_m$ . Note the points at  $D_m$  larger than 2.5 mm in Fig.9 are for the DSD onset where significant different DSDs appear. Estimated values of  $D_m$  from the look-up table of  $\mu_{table}=1, 3$  and 6 are compared (Fig. 12). Symbols of black circles are  $D_m^{Est1}$ , green squares are  $D_m^{Est2}$  using the LUT of  $\mu_{table}=1$ , red circles are estimated from  $\mu_{table}=3$ , and blue triangles are estimated from  $\mu_{table}=6$ . Corrected values from  $\mu_{table}=6$  are still underestimated but are shown to be improved. The reason of this is that the shapes of the simulated DSDs are similar to the Gamma function of larger values of  $\mu$  than that of  $\mu_{table}=3$ . This figure suggests that selection of appropriate LUT is critical for accurate estimation. This issue will be discussed in 4.3.

420

425



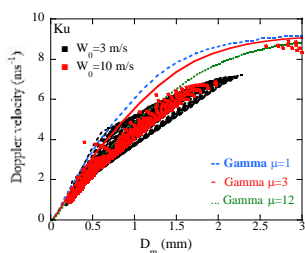
430



435

**Fig. 9** Comparisons of the estimated  $D_m$  with the model values at Ku-band for convective rain ( $W_0=10 \text{ ms}^{-1}$ ). Estimated  $D_m$  without correction (black circles: Est1) and with correction (red squares: Est2) are plotted.

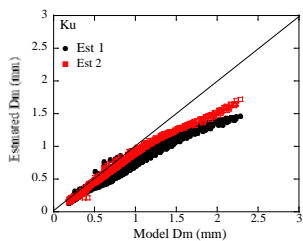
440



445

**Fig. 10** Relationships of  $D_m$  and the Doppler velocities of simulated DSDs (black square:  $W_0=3 \text{ ms}^{-1}$ , red:  $10 \text{ ms}^{-1}$ ) and of the Gamma function (blue:  $\mu=1$ , red:  $\mu=3$ , green:  $\mu=12$ ).

450



455

**Fig. 11** As in Fig.9 but for data of  $W_0=3 \text{ m}^{-1}$ .

460

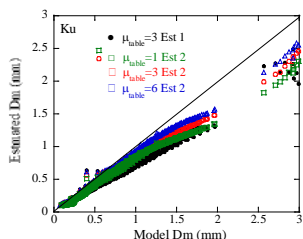


**Fig. 12** As in Fig. 9 but the retrieved  $D_m$  using the look-up table of  $\mu_{table}=1, 3$  and  $6$  are compared.



## 465 4.2 A method for W-band radar

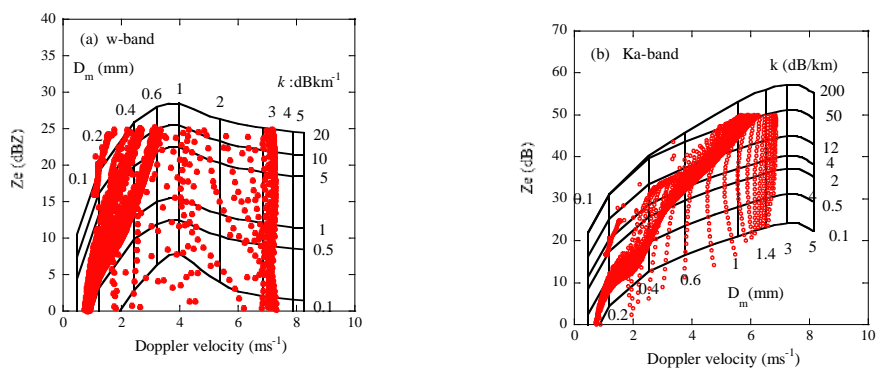
In the previous section, the method to estimate  $D_m$  for Ku-band Doppler radar was described. The specific attenuation monotonically increases with  $D_m$  at this frequency. Whereas, the amplitude of  $k$  increases with  $D_m$ , reaching maximum at about  $D_m=1\text{mm}$ , and then decreases for W-band (Fig.7). This is because that received signals from the CPR operated at W-band are almost in the Mie regime while those for Ku-band are almost in the Rayleigh regime. This feature requires the  
470 modification of the method for W-band. In this section, we will show the modified algorithm to derive  $D_m$  and examine the potential of the method in the measurements of rain with the CPR.

Figure 13 is the same as Fig.8 but for W-band (a) and Ka-band (b). The space-borne Ka-band Doppler radar is not currently planned but is added to examine the method for more frequencies. The DSD is assumed to be the gamma function of  $\mu = 3$  as in Fig.8. The horizontal lines represent  $Z_e$  and  $V_d$  that result for specified values of  $k$  and the vertical lines represent the  
475 values for specified values of  $D_m$ . For W-band, the horizontal lines increase with  $V_p$  below about  $4\text{ ms}^{-1}$  and then slowly decrease because of the Mie effects. Unfavourable features of Fig.13(a) are that double solutions of the estimated  $D_m$  are possible when determining the optimum value of  $D_m$  by changing  $V_p$ . In addition, the slight change of  $k$  with  $V_p$  above about  $4\text{ ms}^{-1}$  need considerable high accurate observations of  $k$ . Similar features are also shown in Ka-band (b). To avoid such difficulties, the radar reflectivity factor ( $Z$ :  $Z_e$  for Rayleigh regime) instead of  $Z_e$  for W and Ka-band is used. The reflectivity  
480 factor  $Z$  is determined from the measured  $Z_e$  and  $V_p$  using the LUT. This may lead to additional errors in the estimation. We, however, decided to this method to avoid uncertainties in the use of  $Z_e$  mentioned above. For  $D_m < 1\text{ mm}$ ,  $Z_e$  can be directly used, but  $Z$  is used for whole  $D_m$  in this study. Generally,  $Z$  is linearly related to  $Z_e$  for near the Rayleigh regime. For W-band, however, the relationship of  $Z$  and  $Z_e$  is not simple. The reflectivity factor  $Z$  is linearly related to  $Z_e$  for  $Z_e < 30\text{dBZ}$  depending on DSD but is considerably larger than  $Z_e$  for larger  $D_m$ . This may not be serious because the retrieval of  $D_m$   
485 would be limited to light rain of  $Z_e$  about less than 20-25 dBZ ( $Z$ : 20-50dBZ depending on  $D_m$ ) for W-band as mentioned earlier but is serious for some cases such as DSD of small number concentrations with large rain drops. To convert the measured reflectivity (attenuated corrected values) to  $Z$ , the lookup-tables were prepared for  $Z$ ,  $Z_e$  and  $V_p$  for DSD of the gamma function of  $\mu$  (eg. 3). The reflectivity factor  $Z$  corresponding to the measured  $Z_e$  is calculated from the measured  $Z_e$  and  $V_p$  using the table for various values of  $D_m$  less than 2.2 mm. Note that unknown values of  $D_m$  are not used for the  
490 conversion.

Fig.14 is the same as Fig.13 but for  $Z$ . The horizontal lines increase monotonically even for W-band. The circle symbols shown in the figure indicate the simulated values of  $Z$  and  $V_p$  in the convective rain (for  $\text{LWC} > 0.1\text{ gm}^{-3}$ ). The DSD's that evolved from the weak initial upward velocities as  $W_0=3$  and  $5\text{ ms}^{-1}$  are plotted instead of  $10\text{ms}^{-1}$  for Ku-band. Smaller reflectivity factor than 25 dBZ which are usually observed with the space-borne W-band radars and 40dBZ for Ka-band, are  
495 shown. From these figures,  $D_m$  can be determined from the measured  $Z_e$ ,  $k$  and  $Z$  similar to the process for Ku-band. Changing the measured Doppler velocity and find the optimum value of  $V_p$  at which the estimated  $k$  matches the observed value. Figure 15 shows the flow of the retrieval algorithm.



500

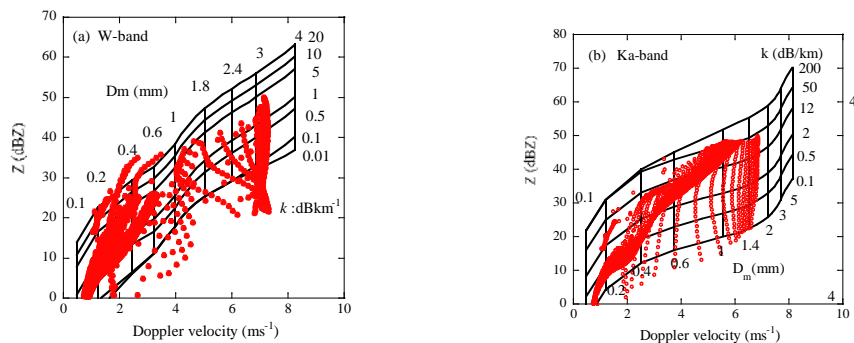


505

510

Fig. 13 As in Fig. 8 but for W (a) and Ka-band (b).

515



520

525

Fig. 14 As in Fig.13 but the Rayleigh scattering equivalent reflectivity factor Z is used instead of Z<sub>e</sub>.

530



535 The Ku-band Doppler radar can detect heavy convective rain up to  $Z_e=40-50\text{dBZ}$ . Simulated data for the initial updraft velocity of  $10\text{ ms}^{-1}$  are appropriate and were used for the validation. Whereas, W-band radar detects light rain of  $Z_e$  about 20-25 dBZ and near top of intense rain layer. Validation was, therefore, performed using the simulated data of the initial upward velocities of  $0.3$  and  $0.5\text{ ms}^{-1}$  for which DSDs of many weak rain events appear. Figure 16a is a similar relationship to Fig.2 but shows the scatter plots of the measured Doppler velocities ( $V_p$ ) and the reflectivity factors ( $Z_m$ ) from the CPR. Most  $Z_m$  are less than 20 dBZ even for higher values of  $V_p$ . Note that values without attenuation correction and unfolding correction are plotted. Therefore, the Doppler velocities are limited to the Nyquist velocity of  $5-6\text{ ms}^{-1}$ . Figure 16b is the same as Fig16(a) but shows the scatterplots of  $V_p$  and  $Z_e$  calculated from the simulated DSDs. The data of  $Z_e$  less than 25dBZ are plotted. For these weaker  $W_0$ , the DSDs similar to the CPR measurements except for higher values of  $V_p$  are obtained. These data were used for the validation of the retrieval for W-band in which primarily measures weak rain. Simulated data for  $W_0=10\text{ ms}^{-1}$  were also used but were limited number for  $Z_e < 25\text{dbZ}$ .

545

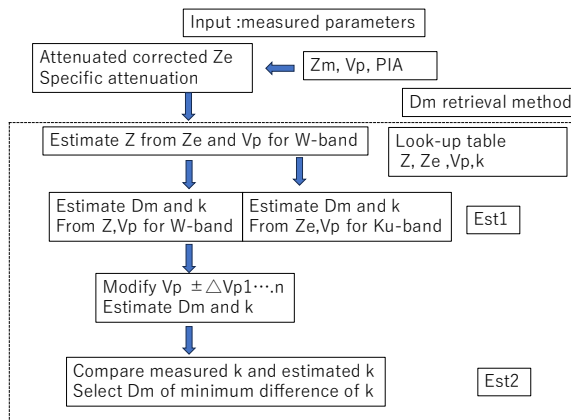
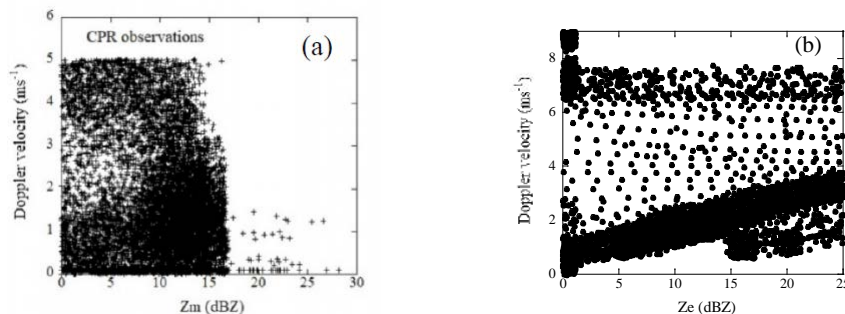


Fig. 15 Retrieval algorithm flow diagram of  $D_m$

550



555

560

**Figure 16** Scatter plot of the Doppler velocities and the reflectivity factor measured with the CPR (a) and simulated (b).

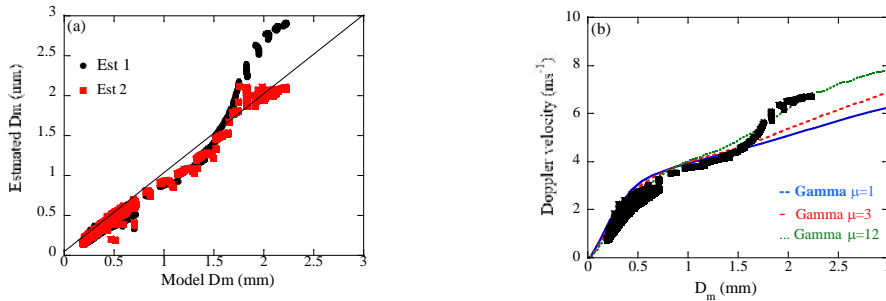
Figure 17 shows the retrieved and calculated (model) values of  $D_m$  for W-band (a). The vertical velocities of the atmosphere are zero for most data. The simulated data with  $W_0=3\text{ms}^{-1}$  are applied. Black circles represent uncorrected values of  $D_m$  ( $D_m^{Est1}$ ), while red square symbols represent the corrected  $D_m$  ( $D_m^{Est2}$ ) estimated using the measured values of  $Z_m$ ,  $k$  and  $V_p$ . For small values of  $D_m$  less than 1.5 mm, both values of  $D_m^{Est1}$  and  $D_m^{Est2}$  agree well with the model values. However, for large  $D_m$ ,  $D_m^{Est1}$  differs significantly from the model  $D_m$ . For  $D_m$  larger than 1.5 mm, values of  $D_m^{Est1}$  are overestimated, which is the opposite of the results in Ku-band (Fig.9). Since these data are considered to be in still air, these discrepancies likely arise from the differences between the measured DSD and the DSD used in the LUT in Figs. 13 and 14. Figure 17(b) shows the relationships of  $V_p$  and  $D_m$  obtained from the simulated DSD (black square) which is a measure to identify DSD. The relationships for the Gamma function of  $\mu = 1$  (blue), 3 (red) and 12 (green) are also plotted. This figure shows that the model values of  $V_p$  are significantly larger than the those of the LUT used in the estimation ( $\mu = 3$ ) for  $D_m > 1.5$  mm, overestimating  $D_m^{Est1}$  which is opposite to the Rayleigh regime. Despite these deviations, the corrected values of  $D_m^{Est2}$  significantly reduce errors and agree well with the model values. This is because the method can compensate the effect of DSD on the retrieved  $D_m$  to some degree as well as the air motion. The data of large  $D_m$  are primarily associated with the DSD onset in which large values of  $D_m$  appear in the initial stage of rain and account for less than 5 % of all data.

Figure 18 is the same as Fig.17 but for Ka-band. Data of  $W_0=3 \text{ ms}^{-1}$  are plotted. For  $D_m < 1$  mm, both estimated values of  $D_m^{Est1}$  and  $D_m^{Est2}$  agree well with the model values. However, for  $D_m > 1.5$  mm, retrieved  $D_m^{Est1}$  tends to underestimate which is opposite of the result for W-band but is similar to the result for Ku-band (Fig.9). In this frequency, the reflectivity both in the Rayleigh regime and the Mie regime coexist depending on the size of raindrops. The errors in the estimated  $D_m$  may be small compared with the cases for Ku and W-band. Figure 18(b) is the same as Fig.17(b) but for Ka-band. This figure is similar to the relationship for Ku-band. Smaller values of  $V_p$  result in underestimation of  $D_m^{Est1}$ .

585

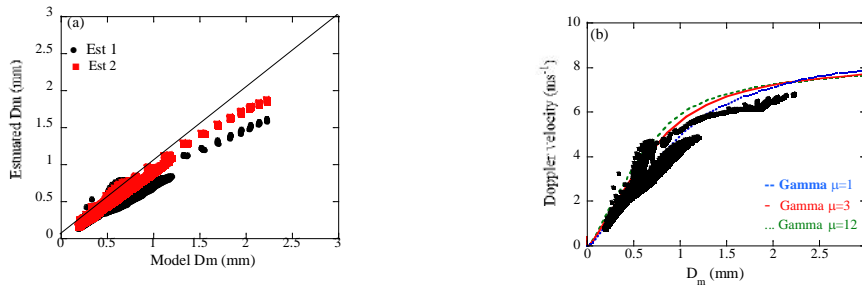


590



**Fig. 17** Comparisons of the estimated  $D_m$  and the model values at W-band (a). Estimated  $D_m$  without correction (black circles: Est1) and with correction (red squares: Est2) are plotted. The Relationships of  $D_m$  and the Doppler velocities of the simulated DSDs, and of the Gamma function ( $\mu=1$ : blue, 3: red, 12: green) are plotted (b).

600



605

**Fig. 18** As in Fig.17 but for Ka-band.

### 4.3 Selection of more appropriate LUT for Ku-band

In the retrieval algorithm, the Mie calculations are performed for the Gamma DSDs of various values of  $\mu$  to prepare the look-up tables (LUT). In each LUT, values of  $Z_e$ ,  $V_p$ ,  $k$ , rain rate ( $R$ ), and  $R/Z_e$  for various values of LWC and  $D_m$  are stored. Selecting an LUT and estimate  $D_m$ . In radar algorithms to estimate rain properties, the Gamma DSD with a value of  $\mu$  fixed at 3 is often used. This paper also employed such an LUT. This LUT yields generally good estimation results for DSDs of  $D_m$  less than 0.5-1.5 mm which are common in many rain events. There are, however, some DSDs of larger  $D_m$  than 1.5 mm which result in bias errors in the estimation results. Thus, the accuracy of the retrieved  $D_m$  depends on the DSD applied in the LUT. In this section, we will describe a technique to select a more appropriate DSD applied in the LUT to achieve more accurate estimation in Ku-band.

As shown in Fig.10, the relationship between  $V_p$  and  $D_m$  is a measure of DSD and allows estimation of  $\mu$  close to the actual DSD but cannot be used here. As another measure of DSD, we utilize the dependence of the relationship between  $Z_e$  and rain



rate on  $D_m$  instead. The rain rate will be derived from the measured reflectivity factors and PIA without  $V_p$  as in the single  
 620 frequency algorithm in GPM. In this paper, rain rate was calculated from the simulated DSD. First, estimate  $D_m^{Est1}$  and  $D_m^{Est2}$   
 using the LUT of the initial value of  $\mu$  ( $=\mu_0$ ). Next, select the ratio of  $Z_e$  to rain rate  $(Z_e/R)^{LUT}$  for  $D_m^{Est2}$  from the LUT. The  
 ratio of the measured reflectivity factor and rain rate,  $(Z_e/R)^{meas}$  is compared with the ratio  $(Z_e/R)^{LUT}$ . If the measured ratio  
 $(Z_e/R)^{meas}$  is larger than the ratio  $(Z_e/R)^{LUT}$  of the initial LUT ( $\mu=\mu_0$ ), the LUT of larger value of  $\mu$  ( $=\mu_{mod}$ ) than  $\mu_0$  is selected as  
 a new LUT and vice versa. A new  $D_m$  (Est3,  $D_m^{Est3}$ ) is re-estimated using the new LUT which is closer to the measured DSD.  
 625 This process is repeated. Fig. 19 shows such estimated  $D_m^{Est3}$  using a new LUT as well as  $D_m^{Est1}$  and  $D_m^{Est2}$  for DSD of  $W_0=10$   
 $ms^{-1}$  (a) and  $W_0=3 ms^{-1}$  (b). The value of  $\mu_0=3$ , and  $\mu_{mod}=1, 6$  or  $9$  are used depending on the ratio. Less underestimated  $D_m^{Est3}$   
 values appear associated with using more appropriate LUT of larger  $\mu$  than  $\mu_0$ . In the estimation, the rain rate calculated from  
 the simulated DSD is applied as mentioned earlier. Note that the rain rate estimate algorithm usually use the measured  
 reflectivity factor and PIA, and therefore is not completely independent of the retrieval algorithm of  $D_m$ . The accuracy of this  
 630 technique depends on the rain rate algorithm and may be needed more validation.

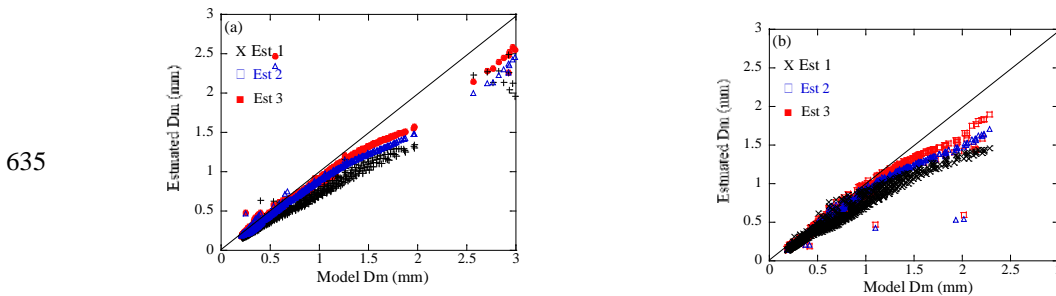


**Fig. 19 Comparisons of the estimated  $D_m$  and model values at Ku-band for DSDs with  $W_0=10 ms^{-1}$  (a) and  $W_0=3 ms^{-1}$   
 640 (b). Estimated  $D_m$  without correction (black circles: Est1) and with correction (blue squares: Est2, red: Est3) are  
 plotted.**

### 5 Error analysis

Having determined  $D_m$ , it is important to examine the uncertainties in  $D_m$  arising from errors in the measured values and the  
 645 retrieval process. First, we examine the uncertainties in  $D_m$  arising from measurement errors in the reflectivity factors,  $V_p$  and  
 $k$ . Even if correct  $V_p$  is given, errors in  $Z_m$  and/or  $k$  result in uncertainties in  $D_m$ . Figure 20 shows the uncertainties in the  
 estimated  $D_m^{Est2}$  with and without measurement errors. The ratios of the estimated  $D_m$  to the model values are plotted for Ku  
 (a) and W-band (b). The ratios without measurement errors (black lines) are lower than unity and decrease with  $D_m$  for Ku-  
 band. For W-band, the ratios increase sharply at about  $D_m=1.5$  mm. These characteristics are associated with the  
 650 discrepancies of DSDs in the measurements and LUT in particular for DSDonset. Positive errors in  $Z_m$  lead to increases in



the ratio and vice-versa for  $k$ . The discrepancies between lines with and without measurement errors indicate effects of the measurement errors on the estimation. When there is a 30% error (linear scale) in  $Z_m$  (green line), the ratios increase by 12 % i.e. 12% errors in the retrieval  $D_m$  arising from about 1 dBZ error in  $Z_m$  for Ku-band. The effects of the measurement errors of 20 % in  $k$  (blue) are smaller as 6 %. For the W-band, there appear smaller effects in particular for larger  $D_m$  where larger changes in  $Z$  with  $D_m$ .

The errors in  $V_p$  are corrected in the retrieval algorithm and do not affect the uncertainties in the retrieved  $D_m$ , but may affect the uncertainties when there exist errors in  $Z_m$  and  $k$ . To assess the uncertainties arising from  $V_p$  errors (or air motion), we examined the retrieval errors when uniform random errors in  $Z_m$  ranging from -30% to +30% and  $k$  ranging from -20% to +20%. Figure 21 shows the mean errors and standard deviations for various  $V_p$  errors. Uncertainties are nearly independent of the  $V_p$  errors for the Ku-band (Fig.21a). For the W-band (Fig.21b), uncertainties increase with  $V_p$  errors due to errors in  $Z$  calculating from  $Z_e$ . The overall uncertainties are small for  $V_p$  errors less than  $\pm 0.5 \text{ ms}^{-1}$ .

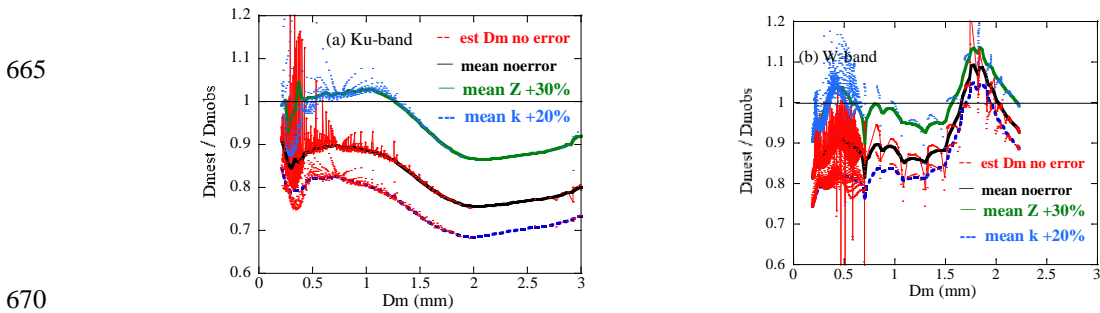


**Fig. 20** The uncertainties in the estimated  $D_m^{Est2}$  with and without measurement errors of 30% in  $Z_m$  and 20% in  $k$  for Ku(a) and W-band (b).

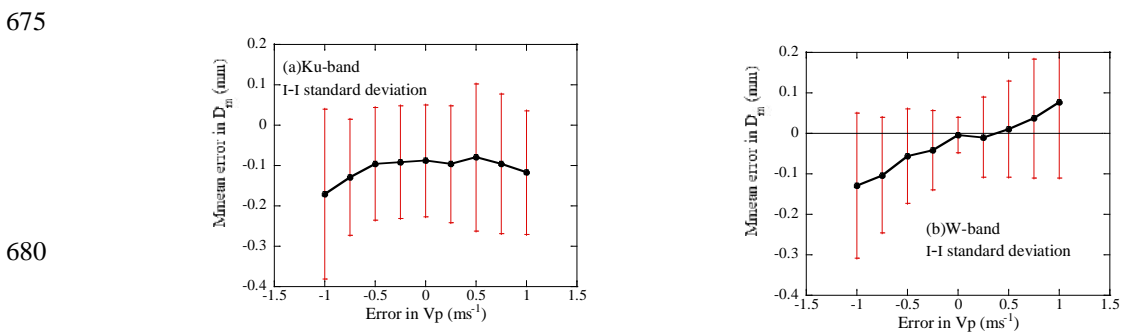


**Fig. 21** Mean errors in the estimated  $D_m^{Est2}$  arising from  $V_p$  errors for Ku (a) and W-band (b). Uniform random errors in  $Z_m$  ranging from -30% to +30% and  $k$  ranging from -20% to +20% are applied.



685 To examine the potential of the method for the practical use, we furthermore estimated  $D_m$  when there are random errors in  
the measured  $Z_e$ ,  $k$ , and  $V_p$ . Figure 22 shows comparisons of the estimated and model values of  $D_m$  for Ku (a, b), Ka (c) and  
W-band (d). Results arising from random errors in  $V_p$  ranging from  $-0.5\text{ms}^{-1}$  to  $+0.5\text{ms}^{-1}$ ,  $Z_e$  from  $-30\%$  to  $+30\%$  (about 1  
dBZ) and  $k$  from  $-20\%$  to  $+20\%$  uniformly are plotted. The black circles represent uncorrected values of  $D_m$  ( $D_m^{\text{Est1}}$ ), i.e.,  
690 the corrected  $D_m^{\text{Est2}}$  for Figs (a, c, d) and  $D_m^{\text{Est3}}$  for (b). There appears large scatter in the estimated  $D_m$  associated with the  
random errors. Following are the mean error (ME) and the root mean square error (RMSE) of the difference between  
estimated and model  $D_m$ s for Est1, Est2 and Est3.

Ku-band:

$$\text{ME}^{\text{Est1}} = -0.1712, \text{ME}^{\text{Est2}} = -0.0908, \text{ME}^{\text{Est3}} = -0.0782$$

695  $\text{RMSE}^{\text{Est1}} = 0.2290, \text{RMSE}^{\text{Est2}} = 0.1613, \text{RMSE}^{\text{Est3}} = 0.1411$

Ka-band:

$$\text{ME}^{\text{Est1}} = -0.1328, \text{ME}^{\text{Est2}} = -0.0765, \text{RMSE}^{\text{Est1}} = 0.1851, \text{RMSE}^{\text{Est2}} = 0.1200$$

W-band:

$$\text{ME}^{\text{Est1}} = -0.0299, \text{ME}^{\text{Est2}} = -0.0336, \text{RMSE}^{\text{Est1}} = 0.1834, \text{RMSE}^{\text{Est2}} = 0.0897.$$

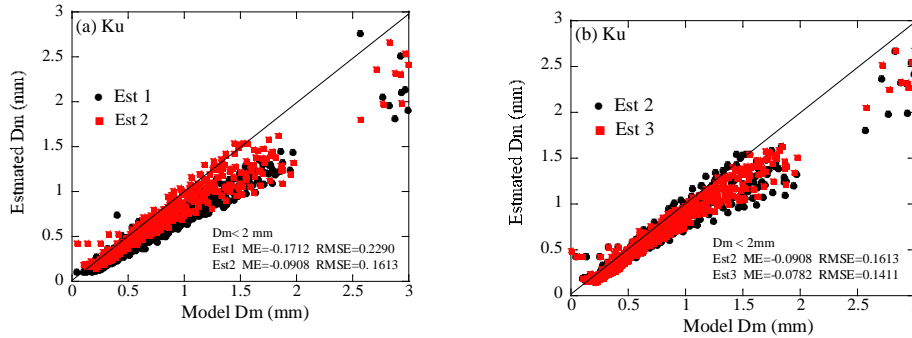
700 The mean errors and RMSE in the estimated  $D_m^{\text{Est2}}$  are improved. Uncertainties over the whole range of  $D_m$  were relatively  
small, as shown above. The retrieval errors in  $D_m$ , however, vary with  $D_m$  because the differences between the measured  
DSDs and those used in the LUT vary with  $D_m$ . Figure 23 shows the percentage errors of the absolute difference between  
retrieved  $D_m$ s and the model values with random errors as in Fig.22. Mean percentage errors and the standard deviations are  
705 plotted for Ku(a), Ka (b) and W-band (c). The mean percentage errors are about 0.15 mm and the standard deviation are less  
than 0.1 mm.

710

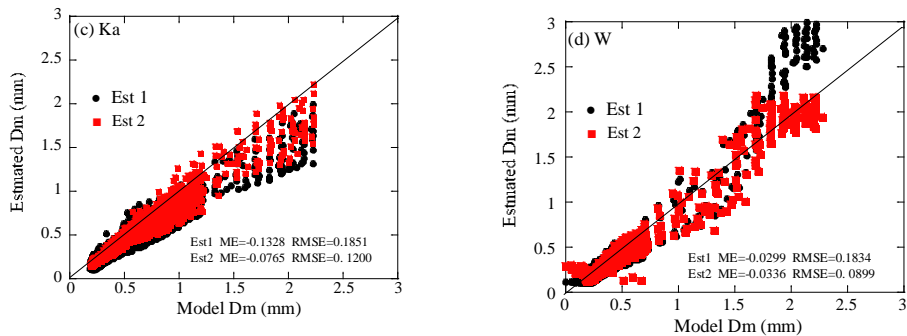
715



720



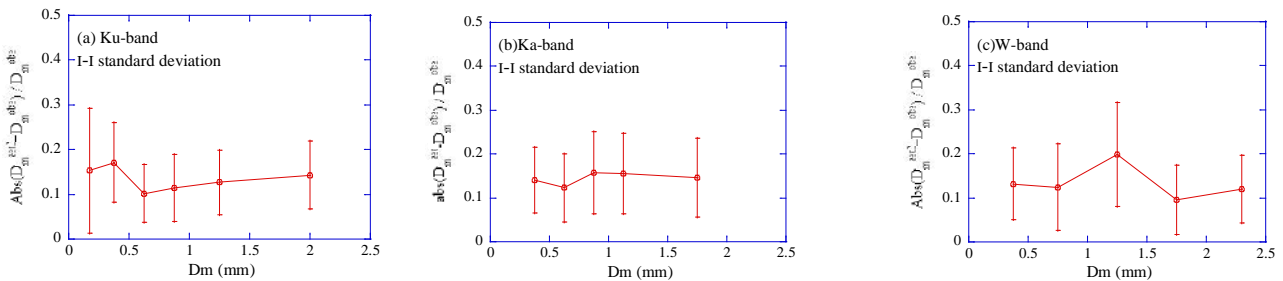
725



730

**Fig. 22 Results of the estimation for random errors in  $V_p$  ranging from  $-0.5\text{ms}^{-1}$  to  $+0.5\text{ms}^{-1}$ ,  $Z_e$  from  $-30\%$  to  $+30\%$  (about 1 dBZ) and  $k$  from  $-20\%$  to  $+20\%$  uniformly for Ku (a), Ku (b), Ka (c) and W-band (d).**

735



740

**Fig. 23 Percentage errors in the retrieved  $D_m$  with random errors in  $Z_e$ ,  $k$ , and  $V_p$  as in Fig.22 for Ku (a), Ka(b) and W-band (c). The ratio of the absolute differences between retrieved and model  $D_m$  to the model  $D_m$  are plotted.**



## 6 Summary

745 A method to estimate  $D_m$  of rain from the space-borne Doppler radars is presented. The radar-measured Doppler velocity is the reflectivity-weighted values and is affected by the vertical velocity of the atmosphere. When estimating  $D_m$  from the measured Doppler velocity, these effects should be removed from the measured Doppler velocity. To remove these effects, a physically-based algorithm using the specific attenuation  $k$  and the reflectivity factors as well as  $V_p$  was developed. The validation of the retrieval method has been made using simulated rain drop size distributions. A Monte Carlo model was used to evolves DSD by coalescence and breakup in a convective rain. The simulated DSD exhibited significant temporal and vertical variations of DSD during the descent processes associated with the lifecycle of rain. The evolved DSD resembled ground-based polarimetric observations, making it suitable for the validation. The relationships between  $D_m$  and rain rate showed large variability and weak correlation, similar to polarimetric radar observations. Detailed analysis, however, revealed that correlations between  $D_m$  and rainfall rate exist, in relation to the stage of rain. Generally,  $Z_e$  is positively related to the rain rate except for the onset of rain. During the early stage of rain, larger and fewer raindrops appeared in lower altitude associated with the absence of breakup, resulting in a negative correlation and significant different DSD compared to other stages. These features were used to analyse the results of validation in detail.

The validation of the retrieval method of  $D_m$  for various DSDs showed that the estimated values of  $D_m^{\text{Est2}}$  were much better than the estimated  $D_m^{\text{Est1}}$ . For Ku-band, the effects of air motion were well removed, whereas the effects of DSD were difficult to correct due to the Rayleigh scattering regime. Accurate estimation needs appropriate LUTs in which similar DSD to the measured one. A technique to determine more appropriate LUTs is presented using the dependence of  $Z$ - $R$  relationship on  $D_m$  for Ku-band. The retrieved  $D_m$ s were improve using this technique. For W-band, the effects of DSD and the air motion on the Doppler velocity were removed except for DSD in the initial stage of rain. Uncertainties in the retrieved  $D_m$  arising from the measurement errors were examined. Results show that the method yields good performance. The proposed method need attenuation corrected reflectivity factors, the specific attenuation and the Doppler velocity. Accurate measurements of such values need more effort in particular for W-band. Although the estimation is limited for weak rain or near top of rain layer for W-band because of the significant attenuation and the Mie scattering regime, the new method possibly improves our understanding of the rain system with space-borne doppler radar.

770 Acknowledgments.

This work is partially supported by Japan Aerospace Exploration Agency.

775



## Appendix A. Method by Gillespie, (1975) and Seeßelberg et al. (1996)

Gillespie (1975) defined and calculated a probability function  $P(\tau, i, j)$  called the coalescence probability density function, and proposed a method that does not ignore the correlation, instead of calculating number of particles directly. Consider the case where there are well-mixed  $N$  droplets at time  $t$ . The function  $P(\tau, i, j) d\tau$  is the probability that droplets  $i$  and  $j$  will collide in the time interval  $t+\tau$  and  $t+\tau+d\tau$ ,  $d\tau$  is the infinitesimal time. This probability is the product of the probability that no collision occurs in the time interval  $t, t+\tau$ , the probability that a collision occurs between  $t+\tau$  and  $t+\tau+d\tau$  and the probability that no collision of the other particle occurs between  $t+\tau$  and  $t+\tau+d\tau$  and is expressed as follows.

$$P(\tau, i, j) = C_{ij} \exp \left[ - \sum_{k=1}^{N-1} \sum_{l=k+1}^N C_{kl} \tau \right], \quad (A-1)$$

where  $C_{ij} d\tau$  the probability that droplets  $i, j$  will collide in the next infinitesimal time  $d\tau$  which is related to the collection kernel as  $K(m_i, m_j)$  per the volume of well-mixed cloud or rain. Given  $C_{ij}$ , the probability can be obtained without approximation. The collision process is numerically calculated for an arbitrary kernel. Eq. (A-1) is given as

$$P(\tau, i, j) = C_{ij} \exp(-C_0 \tau), \quad (A-2)$$

where  $C_0$  is the total rate for any collision events in the volume  $V$ . In the model by Seeßelberg et al. (1996) in which drop classes are introduced to specify DSD, and  $C_0$  is given as

$$C_0 \equiv V^{-1} \sum_{i=1}^N \sum_{j=i+1}^N K_{ij} N_i N_j + V^{-1} \sum_{i=1}^N K_{ii} \frac{N_i(N_i - 1)}{2}, \quad (A-3)$$

where  $K_{ij}$  is the collision kernel, the probability that particles  $i$  and  $j$  in the volume  $V$  collide. The first term on the right-hand side represents the probability that particles  $i \neq j$  and the second term represents the probability that drops of  $i = j$  collide. The time interval  $\tau$  is determined from (A-2) using uniformly distributed random number ( $\eta$ ) from 0 to 1 as:

$$\tau = -C_0^{-1} \ln \eta. \quad (A-4)$$

The next step is to select colliding droplets ( $i, j$ ). The probability of collision of droplet  $i$  and  $j$ , ( $D_{ij}$ ) is expressed as

$$D_{i,i} \equiv V^{-1} K_{i,i} \frac{N_i(N_i - 1)}{2C_0}, \quad i = j \quad (A-5a)$$

$$D_{i,j} \equiv V^{-1} K_{i,j} N_i N_j / C_0. \quad i \neq j \quad (A-5b)$$

The probability of collision of particle  $i$  with any other droplets,  $D_i$  is as follows.

$$D_i = \sum_{j=i+1}^N [D_{ij} + D_{ii}]. \quad (A-6)$$

The colliding particle  $i$  is determined from the cumulative distribution of  $D_i/C_0$  with respect to droplet  $i$  and a random number. The colliding droplet  $j$  with drop  $i$  is determined from the cumulative distribution of  $D_{ij}/D_i$  and a random number. Create a cumulative distribution for the mass (bin number)  $i$  of  $\sum D_i/C_0$  and determine the mass  $i$  by a random number. In this algorithm, the so-called well-known problem (Bott, 1998) arises: the bin of a newly generated particle by coalescence or breakup is determined but is not known the exact size in the bin. We apply the method by Seeßelberg et al. (1996).



The collection kernel is written as follows:

$$K(r, r') = \pi(r' + r)^2 E_{col} E_{coal} |V_{\infty}(r) - V_{\infty}(r')|, \quad (A - 7)$$

where  $E_{col}$  is the collision efficiency, which is the ratio of collision cross section to the geometric cross section, and  $E_{coal}$  is the coalescence efficiency, which indicates the probability of coalescence of collision particles. In this paper, the collision efficiency is set to be unity considering the fact that the raindrop size is larger than 0.1 mm. The coalescence efficiency was calculated by Low and List (1982a).

$$E_{coal} = a \left(1 + \frac{D_s}{D_L}\right)^{-2} \exp\left(-\frac{b\sigma E_r^2}{S_c}\right). \quad (A - 8)$$

Here,  $D_L$  and  $D_s$  are the diameters of larger and smaller drops, and  $S_c$  is the surface energy of the spherical equivalent of the united drop mass.  $E_r$  is the sum of the collision kinetic energy and the particle surface energy loss due to coalescence.  $\sigma$  is the surface tension of water. Parameter  $a$  and  $b$  are constant values. The effect of turbulence is not considered. The coalescence efficiency by Low and List (1982a) may underestimate the coalescence and result in higher slope in the equilibrium raindrop size distribution (Barthes et al., 2013, Hu and Srivastava, 1995). The shape of DSD significantly varies in vertical as well as in the life stage of rain. The object of the simulation is to create a database of such variations of DSD to examine the method for estimating  $D_m$  from space-borne Doppler radar observations, therefore the coalescence efficiency of Eq.A-8 which has been usually used, was applied. For breakup, the probabilities of the occurrence of the filament, sheet, and disk types were considered. The DSD of each type of breakup was determined by Low and List (1982b). Note, the rate of breakup was assumed to be  $(1-E_{coal})$  and for  $D_L < 0.2\text{mm}$ ,  $E_{coal} = 1$ .

Finally, we will mention statistical fluctuations of the results of the MonDrop. Statistically accurate results may be obtained from several runs between three to 10 (Gillespie, 1975). To determine statistically meaningful results with  $K$  runs, following values are used.

$$\Delta D = \left\{ \frac{1}{K} \sum_{i=1}^K [N_i(x)]^2 - \left[ \frac{1}{K} \sum_{i=1}^K [N_i(x)] \right]^2 \right\}^{\frac{1}{2}}, \quad (A - 9)$$

where  $N_i$  is the Monte Carlo results, such as DSD, LWC, etc. at  $i$  run. If  $\Delta D/N_i \ll 1$ , the result can be considered reliable.

## 830 Appendix B. Estimate atmospheric vertical velocity

We will mention about the atmospheric vertical velocity. Because the method corrects the total effects of  $V_{air}$  and DSD on the estimation,  $V_{air}$  cannot be estimated directly but will be estimated from  $V_P$  and  $V_D$ . The raindrop fall velocity  $V_D$  is usually approximated by  $V_D = a Ze^b$  (EqA). This equation is a good approximation but is less accurate for DSDs containing more larger drops even for Ku-band. Another approach is to use the estimated  $D_m$  as  $V_D = c D_m^d$  (EqB). We examined the fall velocities derived from the relationships of  $V_D - Ze$ , and  $V_D - D_m$  for simulated DSDs. The coefficients  $a$ ,  $b$ ,  $c$ ,  $d$  were determined by non-linear least fitting method. Combined equation of EqA and EqB as  $V_D = a' Ze^{b'} + c' D_m^{d'}$  (EqAB) was also examined. For W-band, the absolute mean error (ME) and the root-mean-square error (RMSE) were 0.23 ms<sup>-1</sup> and 1.39



for EqA, 0.026 and 0.302 for EqB, and 0.002 and 0.283 for EqAB. The ME were not so bad but larger RMSEs appear for EqA than EqB and EqAB. This is because lower values of Ze associated with fewer larger drops in  $D_m > 2.5\text{mm}$  result in underestimated  $V_d$  for EqA. The RMSEs were calculated for data of  $D_m < 2.0\text{mm}$ . Results show that the RMSE are significantly reduced as 0.532 (EqA). For EqB and EqAS, the errors were also slightly improved. For Ku-band, the ME and the RMSE were  $0.21\text{ ms}^{-1}$  and 1.33 for EqA, and 0.055 and 0.498 for EqB. For EqAB, errors are further improved as 0.017 and 0.327. Less errors were obtained comparing with W-band as expected. The atmospheric velocity may be derived from measured  $V_p$  and estimated  $V_D$  using EqB or EqAB except for weak  $V_{air}$ . Note the values of the coefficients depend on the data and are needed more verification.

### Data availability statement.

Simulated data used in the manuscript are available upon request.

### Author contribution:

T. Kobayashi developed the retrieval algorithm. K. Masuda developed MonDROP model. H. Yamauchi and A. Adachi made validations.

### Competing interests:

We declare that they have no conflict of interest.

### References

- Adachi, A., Kobayashi, T., and Yamauchi H.: Estimation of Raindrop Size Distribution and Rainfall Rate from Polarimetric Radar Measurements at Attenuating Frequency Based on the Self-Consistency Principle. *J. Meteor. Soc. Japan*, 93,359-388. <https://doi.org/10.2151/jmsj.2015-020>, 2015
- Atlas, D., Srivastava R. C., and Sekhon R. S.: Doppler radar characteristics of precipitation at vertical incidence. *Rev. Geophys. Space Phys.*, 2, 1-35. <https://doi.org/10.1029/RG011i001p00001>, 1973.
- Battaglia, A., Kollias P., Dhillon R., Rot R., Tanelli S., Lamer K., Grecu M., Lebsock M., Watters D., Mroz K., Heymsfield G., Li L., and Furukawa K.: Spaceborne cloud and precipitation radars: Status, challenges, and ways forward. *Rev. Geophysics*, 10.1029/2019RG000686, 2019.
- Bayewitz, M. H., Yerushalmi J., Katz S., and Shinnar R.: The extent of correlations in a stochastic coalescence process. *J. Atmos. Sci.*, 31,1604-1614. [https://doi.org/10.1175/1520-0469\(1974\)031<1604:TEOCIA>2.0.CO;2](https://doi.org/10.1175/1520-0469(1974)031<1604:TEOCIA>2.0.CO;2) 1974.
- Barthes, L., and Mallet X.: Vertical evolution of raindrop size distribution: Impact on the shape of the DSD. *Atmos. Res.*, 119,13-22. <https://doi.org/10.1016/j.atmosres.2011.07.011>, 2013.
- Berry, E. X., and Reinhardt R. L.: An analysis of cloud droplet growth by collection: Part I. Double distributions. *J. Atmos. Sci.*, 31, 1814-1824. [https://doi.org/10.1175/1520-0469\(1974\)031<1814:AAOCDG>2.0.CO;2](https://doi.org/10.1175/1520-0469(1974)031<1814:AAOCDG>2.0.CO;2), 1974.



- 870 Bringi, V. N., Thurai, M., Nakagawa K., Huang, G. J., Kobayashi, T., Adachi A., Hanado H., and Sekizawa S.: Rainfall Estimation from C-Band Polarimetric Radar in Okinawa, Japan: Comparisons with 2D-Video Disdrometer and 400 MHz Wind Profiler *J. Meteor. Soc. Japan*, 4,705-724, <https://doi.org/10.2151/jmsj.84.705>, 2006.
- Bringi, V. N., Chandrasekar V., Hubbert J., Gorgucci E., Randeu W. L., and Schoenhuber M.: Raindrop size distribution in different climatic regimes from disdrometer and dual-polarized radar analysis. *J. Atmos. Sci.*, 354-365. [https://doi.org/10.1175/1520-0469\(2003\)060<0354:RSDIDC>2.0.CO;2](https://doi.org/10.1175/1520-0469(2003)060<0354:RSDIDC>2.0.CO;2), 2003.
- 875 Bringi, V. N., Williams C. R., Thurai M., and May P. T.: Using Dual-polarized radar and dual-frequency profiler for DSD characterization: A case study from Darwin, Australia, *J. Atmos. Ocea. Technol.*, 2107-2122, 26, 2009. <https://doi.org/10.1175/2009JTECHA1258.1>, 2009.
- Bott, A.: A flux method for the numerical solution of the stochastic collection equation. *J. Atmos. Sci.*, 55, 2284-2293. [https://doi.org/10.1175/1520-0469\(1998\)055<2284:AFMFTN>2.0.CO;2](https://doi.org/10.1175/1520-0469(1998)055<2284:AFMFTN>2.0.CO;2), 1998.
- 880 Chen, F., Zheng X., Wen H., and Yuan Y.T.: Microphysics of convective and stratiform precipitation during the summer monsoon season over the Yangtze-Huaihe river valley, China. *J. Hydrometeor.*, 23, 239-252., DOI: 10.1175/JHM-D-21-0078.1. 2022.
- Gillespi, D.L.: An Exact Method for numerically simulating the Stochastic Coalescence process in a Cloud, *J. Atmos. Sci.*, 32, 1977-1989. [https://doi.org/10.1175/1520-0469\(1975\)032<1977:AEMFNS>2.0.CO;2](https://doi.org/10.1175/1520-0469(1975)032<1977:AEMFNS>2.0.CO;2), 1975.
- 885 Guangheng Ni, Y.M., Chandrasekar V. C., Tian F., and Chen H.: Statistical characteristics of raindrop size distribution during rainy seasons in the Beijing urban area and implications for radar rainfall estimation. *Hydro. Earth Syst. Sci.*, 23, 4153-4170. <https://doi.org/10.5194/hess-23-4153-2019>, 2019.
- Houze, R. A.: Cloud dynamics, Academic Press, 406pp., ISBN-10 0123742668, 2014, 1993.
- 890 Hu, Z. L., and Srivastava R. C.: Evolution of raindrop size distribution by coalescence, breakup and evaporation -theory and observations. *J. Atmos. Sci.*, 52, 1761-1783, [https://doi.org/10.1175/1520-0469\(1995\)052<1761:Eorsdb>2.0.Co;2](https://doi.org/10.1175/1520-0469(1995)052<1761:Eorsdb>2.0.Co;2), 1995.
- Iguchi, T., Kozu T., Meneghini R., Awaka J., and Okamoto K. : Rain profiling algorithm for the TRMM precipitation radar. *J. Appl. Meteor.*, 39, 2038-2052. [https://doi.org/10.1175/1520-0450\(2001\)040<2038:RPAFTT>2.0.CO;2](https://doi.org/10.1175/1520-0450(2001)040<2038:RPAFTT>2.0.CO;2), 2000.
- 895 Khain, A. Ovtchinnikov M. M., Pinsky M., Pokrovsky A., and Krugliak H.: Notes on the state-of-the-art numerical modeling of cloud microphysics, *Atmos. Res.*, 55, 159-224, [https://doi.org/10.1016/S0169-8095\(00\)0064-8](https://doi.org/10.1016/S0169-8095(00)0064-8), 2000.
- Kollias, P., Treserras B. P., Battaglia A., Borque P. C., and Tatarevic A.: Processing reflectivity and Doppler velocity from EarthCARE's cloud-profiling radar: the C-FMR, C-CD and C-APC products, *Atmos. Meas. Tech.*, 16, 1901-1914. <https://doi.org/10.5194/amt-16-1901-2023>, 2023.
- 900 Kobayashi, T., and Adachi A.: Measurements of raindrop breakup by using UHF wind profilers, *Geophys. Res. Lett.*, 4071-4074. <https://doi.org/10.1029/2001GL013254>, 2001
- Kobayashi T., and Adachi A.: Retrieval of Arbitrary shaped raindrop size distributions from wind profiler measurements, *J. Atmos. Oceanic Technol.*, 22, 433-442. <https://doi.org/10.1175/JTECH1705.1>, 2005.



- Kobayashi T., and Nomura M., Adachi A., Sugimoto S., Takahashi N., and H. Hirakuchi H. : Retrieval of attenuation  
905 profiles from the GPM dual-frequency radar observations, *J. Meteor. Soc. Japan*, 99, 603-621.doi:10.2151/jmsj.2021-030, 2022.
- Langmuir, I.: The production of rain by a chain reaction in cumulus clouds at temperatures above freeze. *J. Meteor.*, 5,175-192. [https://doi.org/10.1175/1520-0469\(1948\)005<0175:TPORBA>2.0.CO;2](https://doi.org/10.1175/1520-0469(1948)005<0175:TPORBA>2.0.CO;2), 1948.
- List, R., and McFarquhar G. M.: The role of breakup and coalescence in the three-peak equilibrium distribution of raindrops.  
910 *J. Atmos. Sci.*, 47,2274-2292. [https://doi.org/10.1175/1520-0469\(1990\)047<2274:TROBAC>2.0.CO;2](https://doi.org/10.1175/1520-0469(1990)047<2274:TROBAC>2.0.CO;2), 1990.
- Long, A.: Solutions to the droplet collection equation for polynomial kernels. *J. Atmos. Sci.*,31, 1040-1052. [https://doi.org/10.1175/1520-0469\(1974\)031<1040:STTDCE>2.0.CO;2](https://doi.org/10.1175/1520-0469(1974)031<1040:STTDCE>2.0.CO;2), 1074.
- Low T. and List R.: Collision, Coalescence and Breakup of Raindrops. Part I: Experimentally Established Coalescence Efficiencies and Fragment Size Distributions in Breakup. *J. Atmos. Sci.*, 39, 1591-1606. 1982a
- 915 Low T. and List R.: Collision, Coalescence and Breakup of Raindrops. Part II: Experimentally Established Coalescence Efficiencies and Fragment Size Distributions in Breakup. *J. Atmos. Sci.*, 39, 1607-1618. [https://doi.org/10.1175/1520-0469\(1982\)039<1591:CCABOR>2.0.CO;2](https://doi.org/10.1175/1520-0469(1982)039<1591:CCABOR>2.0.CO;2) , 1982b.
- Matrosov, S. Y.: Characteristic raindrop size retrieval from measurements of difference in vertical Doppler velocities at Ka and W-band radar frequencies. *J. Atmos. Oceanic Technol.*, 34,65-71, Doi:10.1175/JTECH-D-16-0181.1, 2017.
- 920 Meneghini, R., and Nakamura K.: Range profiling of rain rate by airborne weather radar. *Remote Sense. Environ.*, 31, 193-209. [https://doi.org/10.1016/0034-4257\(90\)90089-5](https://doi.org/10.1016/0034-4257(90)90089-5), 1990.
- Mroz, K., Battaglia A., Kneifel S., D’Adderio L. P., and Neto J. D.: Triple-frequency Doppler retrieval of characteristic raindrop size, *Earth and Space Sci.*, 1-17, doi:10.1029/2019EA000789, 2020.
- Mroz, K., B.P. Treserras, Battaglia A., P. Kollias, A. Tatarevic and F. Tridon: Cloud and precipitation microphysical  
925 retrievals from the EarthCARE cloud profiling radar: the C-CLD product, *Atmos. Meas. Tech.*, 16,2865-2888, <https://doi.org/10.5194/amt-16-2865-2023>, 2023
- MaClatchey, R. A., Fenn R. W., Selby, J. E. A., Volz, F. E., and Garing, J. S., 1971: Optical properties of the atmosphere, AFCRL -71-0279.
- Pruppacher, H. R., and Klett J. D.: *Microphysics of Clouds and Precipitation*. Kluwer Academic, 954 pp **ISBN-10:**  
930 0792342119, 1997.
- Rogers, R. R.: Raindrop collision rates. *J. Atmos. Sci.*, 46,2469-2472, [https://doi.org/10.1175/1520-0469\(1989\)046%3C2469:RCR%3E2.0.CO;2](https://doi.org/10.1175/1520-0469(1989)046%3C2469:RCR%3E2.0.CO;2),1989.
- Sato K., Okamoto H., Yamamoto M., K., Fukao S., Kumagai H., Ohno Y., Horie H., and Abo M.: 95-GHz Doppler rada and lidar synergy for simultaneous ice microphysics and in-cloud vertical air motion retrieval., *J. Geophys. Res.*, 114,  
935 D03203, doi:10.1029/2008JD010222, 2009.
- Seeßelberg, M., Trautmann T, and Thorn M. : Stochastic simulations as a bench-mark for mathematical methods solving the coalescence equation. *Atmos. Res.*,40, 33-48. [https://doi.org/10.1016/0169-8095\(95\)00024-0](https://doi.org/10.1016/0169-8095(95)00024-0), 1996.



- Seto S., Iguchi T., Meneghini R., Awaka J., Kubota T., Masaki T. and Takahashi N.: The Precipitation Rate Retrieval Algorithms for the GPM Dual-frequency Precipitation Radar. *J. Meteor. Soc. Japan*, 39-71.
- 940 <https://doi.org/10.2151/jmsj.2021-011>, 2021.
- Shusse Y., Maki M., Shimizu S., Iwamami K., Maesaka T., Suzuki S., Sakurai N., and Misumi R.: Relationship between precipitation core behavior in cumulonimbus clouds and surface rainfall intensity on 18 August 2011 in the Kanto region, Japan. *J. Meteor. Soc. Japan*, 93,215-228, DOI:10.2151/jmsj.2015-012, 2015.
- Wehr, T., Kubota T, Tzeremes G., Wallace K., Nakatsuka H., Ohno Y., Koopman R., Rusli S., Kikuchi M., Eisinger M.,  
945 Tanaka T., Taga M., Deghaye P., Tomita R., and Bernaerts D.: The EarthCARE mission– science and system overview, *Atmos. Meas. Tech.*, 16, 3581–3608, <https://doi.org/10.5194/amt-16-3581-2023>, 2023.
- Williams C. R., Beauchamp R. M., and Chandrasekar V.: Vertical air motions and raindrop size distributions estimated using mean Doppler velocity difference from 3- and 35-GHz vertically pointing radars. *IEEE Trans. Geo. Rem. Sens.*, 54,6048-6060. doi:10.1109/TGRS.2016.2580526, 2016.
- 950 Yamaji, M., Takahashi H. G., Kubota T., Oki R., Hamada A., and Takayabu Y. N.: 4-year climatology of global drop size distribution and seasonal variability observed by spaceborne dual-frequency precipitation radar., *J. Meteor. Soc. Japan*, 98, 755-773. Doi:10.2151/jmsj.2020-038, 2021.